UNIVERSITÀ DI PARMA
ARCHIVIO DELLA RICERCA

University of Parma Research Repository

Binary black hole coalescence in the large-mass-ratio limit: The hyperboloidal layer method and waveforms at null infinity

note finali coverpage

(Article begins on next page)

13 August 2025

Binary black hole coalescence in the large-mass-ratio limit: the hyperboloidal layer method and waveforms at null infinity

Sebastiano Bernuzzi,[1] Alessandro Nagar,[2] and Anıl Zenginoğlu[3]

[1] *Theoretical Physics Institute, University of Jena, 07743 Jena, Germany*
[2] *Institut des Hautes Etudes Scientifiques, 91440 Bures-sur-Yvette, France*
[3] *Theoretical Astrophysics, California Institute of Technology, Pasadena, California, USA*

We compute and analyze the gravitational waveform emitted to future null infinity by a system of two black holes in the large mass ratio limit. We consider the transition from the quasi-adiabatic inspiral to plunge, merger, and ringdown. The relative dynamics is driven by a leading order in the mass ratio, 5PN-resummed, effective-one-body (EOB), analytic radiation reaction. To compute the waveforms we solve the Regge-Wheeler-Zerilli equations in the time-domain on a spacelike foliation which coincides with the standard Schwarzschild foliation in the region including the motion of the small black hole, and is globally hyperboloidal, allowing us to include future null infinity in the computational domain by compactification. This method is called the hyperboloidal layer method, and is discussed here for the first time in a study of the gravitational radiation emitted by black hole binaries. We consider binaries characterized by five mass ratios, $\nu = 10^{-2,-3,-4,-5,-6}$, that are primary targets of space-based or third-generation gravitational wave detectors. We show significative phase differences between finite-radius and null-infinity waveforms. We test, in our context, the reliability of the extrapolation procedure routinely applied to numerical relativity waveforms. We present an updated calculation of the final and maximum gravitational recoil imparted to the merger remnant by the gravitational wave emission, $v_{\rm kick}^{\rm end}/(c\nu^2) = 0.04474 \pm 0.00007$ and $v_{\rm kick}^{\rm max}/(c\nu^2) = 0.05248 \pm 0.00008$. As a self consistency test of the method, we show an excellent fractional agreement (even during the plunge) between the 5PN EOB-resummed mechanical angular momentum loss and the gravitational wave angular momentum flux computed at null infinity. New results concerning the radiation emitted from unstable circular orbits are also presented. The high accuracy waveforms computed here could be considered for the construction of template banks or for calibrating analytic models such as the effective-one-body model.

I. INTRODUCTION

Compact binaries with large mass ratios are primary targets for space-based detectors of gravitational waves (GWs), like the Laser Interferometer Space Antenna (LISA) [1, 2] (or the similar ESA-led mission), and for third-generation ground-based detectors, like the planned Einstein Telescope [3]. For example, the quasi-adiabatic inspiral of extreme-mass-ratio (EMR) binaries, i.e. of mass ratio $\nu \sim 10^{-6}$, is interesting for LISA (see e.g. [4]), while the merger of intermediate-mass-ratio (IMR) binaries, $\nu \sim 10^{-2} - 10^{-3}$, is in the band of sensitivity of the Einstein Telescope [5]. The theoretical modelling of such sources is a difficult task since neither numerical relativity (NR) simulations (due to their computational cost [6, 7]), nor standard post-Newtonian (PN) techniques [8] (due to the strong-field, high-velocity regime) can be applied.

Black-hole perturbation theory is instead the natural tool to model large mass ratio binaries [9–19]. The relative dynamics of the binary is described by the motion of a particle (representing the small black hole) in a fixed background, black-hole spacetime (representing the central, supermassive black hole). The dynamics of the particle is driven away from geodesic motion by the action of radiation reaction through a long, quasi-adiabatic inspiral phase up to the nonadiabatic plunge into the black hole. For what concerns nonconservative (dissipative) effects only, they can be modeled either numerically, for example in the adiabatic approximation, (e.g. as in [9, 20, 21] and references therein) or analytically, using PN-resummed results (à la effective-one-body), going in fact beyond the adiabatic approximation [10, 18, 22, 23]. Gravitational self-force calculations [24–29] can provide corrections to the particle conservative and nonconservative dynamics at next-to-leading/higher order in the mass (away from geodesic motion), although the field is not ready yet for waveform production. Finally, a very promising (semi)-analytical approach to describe the binary dynamics and to produce waveform template banks (for *any* mass ratio, including EMR and IMR binaries) is the effective-one-body (EOB) model [30–39]. The EOB approach is intrinsically nonadiabatic and it is designed to take into account both conservative and nonconservative back-reaction effects, but requires the calibration of some flexibility parameters to account for (yet uncalculated) higher-order effects in the dynamics and waveforms [22, 40–46].

The most important output of these studies is the GW signal which encodes the gauge-invariant information about the source as it should be seen by detectors. Gravitational waves are rigorously and unambiguously defined only at null infinity. Numerical computations, however, are confined to finite grids. A theoretical problem is thus to model and to compute the waveforms at

null infinity, as seen by a far-away idealized observer.

This problem is prominent especially in NR simulations. When an asymptotically Cauchy foliation of the spacetime is employed, the waveforms are typically extracted on coordinate spheres at finite distances from the source. To compute waveforms at null infinity postsimulation techniques are applied. Extrapolation to infinite extraction radius [47–51] proved to be sufficiently robust and accurate, though somehow delicate due to ambiguities introduced by the gauge dynamics and the choice of a fiducial background. An unambiguous procedure based on the Cauchy-characteristic extraction (CCE) method [52–54] has recently been implemented [55–57] to extract waveforms from binary black hole mergers of comparable masses. Although the set up of initial data for the characteristic evolution is intricate [58], the method successfully provides waveforms from binary black hole mergers at null infinity and permits to crosscheck the standard extrapolation procedure.

An alternative approach that does not require postprocessing is to employ spacelike surfaces that approach null infinity. Such surfaces are called hyperboloidal because their asymptotic behavior resembles that of standard hyperboloids in Minkowski spacetime [59]. Hyperboloidal foliations have already been considered in the early days of numerical relativity and were expected to be suitable for studying gravitational radiation [60–63]. The hyperboloidal initial value problem for the Einstein equations has been analyzed by Friedrich [59, 64]. His conformally regular field equations have been implemented numerically in certain test cases (for reviews see [65, 66]).

More recently, alternative hyperboloidal formulations have been suggested [67–69] that do not exhibit explicit conformal regularity. The only successful numerical implementation of such a formalism is by Rinne in axisymmetry [70]. It is an outstanding question whether this or a similar hyperboloidal approach will lead to generic numerical simulations of black hole spacetimes.

While the numerical properties of the hyperboloidal method for Einstein equations is only poorly understood in the general case, the situation is much clearer in perturbation theory where the background is given. There, the best numerical gauge is to fix the coordinate location of null infinity (scri), as first discussed by Frauendiener in the context of conformally regular field equations [71]. Moncrief presented the first explicit construction of a hyperboloidal scri-fixing gauge for Minkowski spacetime [72] (for numerical implementations see [73–75]). The application of the method in black hole spacetimes proved to be difficult [76–80], until the general construction of suitable hyperboloidal scri-fixing coordinates on asymptotically flat spacetimes has been presented [81]. Since then, hyperboloidal scri-fixing coordinates have been employed in a rich variety of problems concerning black hole spacetimes [22, 82–91].

In particular, hyperboloidal compactification has been applied to solve in time-domain the homogeneous Regge-Wheeler-Zerilli (RWZ) equations [92–96] for metric per-

turbations of a Schwarzschild black hole [86]. This work showed the efficiency of hyperboloidal compactification as applied to the RWZ equations and discovered that the asymptotic formula relating the curvature perturbation ψ_4 to the gravitational strain is invalid for the polynomially decaying solution even at large distances used for standard waveform extraction, thereby emphasizing the importance of including null infinity in numerical studies of gravitational radiation.

The solution of the *inhomogeneous* RWZ equations on a hyperboloidal slicing of the Schwarzschild spacetime is discussed in this paper for the first time. The presence of a compactly supported matter source, such as a pointparticle [11, 12] or a test-fluid [18, 97–99], implies modifications. It may be desirable to use standard techniques in a compact domain including the central black hole and the matter dynamics. The hyperboloidal method shall then be restricted to the asymptotic domain only, so that standard coordinates for matter dynamics can be employed. Such a restricted hyperboloidal compactification provides the idealized waveform at null infinity, avoids outer boundary conditions, and increases the efficiency of the numerical computation without changing the coordinate description of matter dynamics.

A convenient technique to achieve this, called the *hyperboloidal layer method*, has been introduced in [100]. A hyperboloidal layer is a compact radial shell in which the spacelike foliation approaches null infinity and the radial coordinate is compactifying. By properly attaching such a layer to a standard computational domain, one makes sure that outgoing waves are transported to null infinity and no outer boundary conditions are needed. An intuitive prescription for the construction of a suitable hyperboloidal layer, that we describe in Sec. III B, is to require that the spherically outgoing null surfaces have the same representation in the layer coordinates as in the interior coordinates. Because the hyperboloidal layer is practically attached to an existing computational domain, only minimal modifications to current numerical infrastructures are needed for its implementation.

In this paper we apply the hyperboloidal layer method to improve the quality of recently computed RWZ waveforms emitted by the coalescence of (circularized) blackhole binaries in the test-particle limit [10] (hereafter Paper I) (see also Refs. [18, 22, 23]). The central new result of this paper is the computation of highly accurate gravitational waveforms at future null infinity ($\mathscr{I}^+$) with an efficient and robust method. As in Paper I, the relative motion of the binary is driven by 5PN-accurate, EOB-resummed [39, 101] analytical radiation reaction and we focus on the transition from quasi-adiabatic inspiral to plunge, merger, and ringdown. To span the range between IMR and EMR, we consider five mass ratios, $\nu \equiv \mu/M = 10^{-2,-3,-4,-5,-6}$, where M is the mass of the central Schwarzschild black hole, and μ is the mass of the small compact object approximated as a point particle. We estimate the differences between waveforms extracted at $\mathscr{I}^+$ and waveforms extracted at finite radii,

and we provide an updated estimate of the gravitational recoil previously computed from finite-radius waveforms in Refs. [9, 10]. The availability of $\mathscr{I}^+$ waveforms also allows us to assess, in a well controllable setup, the accuracy of the extrapolation procedure that is routinely applied to NR waveforms.

The new multipolar waveform extracted at $\mathscr{I}^+$ presented here has already been used in Ref. [22] (hereafter Paper II) to obtain several results that are valuable for currently ongoing EOB/NR comparisons: (i) finite-distance effects are significant even at comparatively large extraction radii ($r \sim 1000M$); (ii) the agreement between the EOB-resummed analytical multipolar waveform [39, 101] and the RWZ waveform improves when the latter is extracted at $\mathscr{I}^+$; (iii) the tuning of next-to-quasi-circular corrections to the phase and amplitude of the EOB-resummed (multipolar) waveform improves its agreement with the RWZ waveform during the late-plunge and merger phase (See also Ref. [40] for a similar tuning procedure applied to several black-hole binaries with comparable mass ratios.)

The paper is organized as follows. In Sec. II we briefly recall the model for the relative dynamics of the binary. The construction of the hyperboloidal layer in Schwarzschild spacetime is carried out in Sec. III. We discuss the RWZ equations with and without the hyperboloidal layer in Sec. IV. Details of the numerical implementation are presented in Sec. V. Physical results are collected in Sec. VI, which consists of the following parts. First, we assess the accuracy of our implementation in the case of stable circular orbits, and present new results for unstable circular orbits. We then focus on the gravitational waveforms emitted during the transition from the quasi-circular inspiral through plunge, merger, and ringdown, and we quantify the differences with finite-radius extraction. We discuss the performance of standard techniques to extrapolate the finite-radius waveform to infinite extraction radius. Concluding remarks are presented in Sec. VI. In Appendix A we present convergence tests of the code. In Appendix B we summarize the relations between the RWZ master functions and asymptotic observables. We mainly use geometrized units with $G = c = 1$.

II. RELATIVE DYNAMICS

The relative dynamics of the binary is computed as in Paper I and II; here we review a few elements that are relevant to our study.

The binary dynamics has a conservative part (Hamiltonian) and a dissipative part (radiation-reaction force). The conservative part is described by the $\nu \to 0$ limit of the EOB Hamiltonian (the Hamiltonian of a particle in Schwarzschild spacetime) with the following, dimensionless variables: the relative separation $r = R/M$, the orbital phase φ, the orbital angular momentum $p_\varphi = P_\varphi/(\mu M)$, and the orbital linear momentum $p_{r_*} = P_{r_*}/\mu$, canonically conjugate to the tortoise radial coordi-

nate separation $r_* = r + 2\ln(r/2 - 1)$. The Schwarzschild metric in standard coordinates (t, r) reads

$$g = -A\,dt^2 + A^{-1}\,dr^2 + r^2\,d\sigma^2 , \qquad (1)$$

where $d\sigma^2$ is the standard metric on the unit sphere and $A \equiv 1 - 2/r$. The Schwarzschild Hamiltonian per unit (μ) mass is

$$\hat{H} = \sqrt{A\left(1 + \frac{p_\varphi^2}{r^2}\right) + p_{r_*}^2} . \qquad (2)$$

The expression for the analytically resummed mechanical angular momentum loss (our radiation-reaction force), $\hat{\mathcal{F}}_\varphi$, is accurate at first order in the mass ratio, $\varnothing(\nu)$, and is computed from the 5PN-accurate EOB-resummed waveform of Refs. [10, 23, 39, 101]. Following [10, 18, 23, 102], we use

$$\hat{\mathcal{F}}_\varphi \equiv -\frac{32}{5}\nu\Omega^5 r^4 \hat{f}(v_\varphi), \qquad (3)$$

where $\Omega = d\varphi/dt$ is the orbital frequency, $v_\varphi = r\Omega$ is the azimuthal velocity, and $\hat{f} = F^{\ell_{\max}}/F_{22}^{\mathrm{Newt}}$ denotes the Newton-normalized ($\nu = 0$) energy flux up to multipolar order $\ell_{\max}$, analytically resummed according to Ref. [23, 39]. The resummation procedure is based on a certain multiplicative decomposition of the circularized multipolar gravitational waveform. More precisely, for circular orbits, the energy flux is written as

$$F^{\ell_{\max}} = \sum_{\ell=2}^{\ell_{\max}}\sum_{m=1}^{\ell} F_{\ell m}$$
$$= \frac{1}{8\pi}\sum_{\ell=2}^{\ell_{\max}}\sum_{m=1}^{\ell} (m\Omega)^2 |rh_{\ell m}|^2. \qquad (4)$$

Above, $h_{\ell m}$ is the factorized waveform of [39],

$$h_{\ell m}(x) = h_{\ell m}^{(N,\epsilon)}(x)\hat{S}^{(\epsilon)}(x)T_{\ell m}(x)e^{i\delta_{\ell m}(x)}(\rho_{\ell m}(x))^\ell, \quad (5)$$

where $h_{\ell m}^{(N,\epsilon)}(x)$ represents the Newtonian contribution given by Eq. (4) of [39], $\epsilon = 0$ (or 1) for $\ell + m$ even (odd). The remaining terms are defined as follows: $\hat{S}^{(\epsilon)}$ is the (specific) source, Eqs. (15-16) of [39]; $T_{\ell m}$ is the tail factor that resums an infinite number of leading logarithms due to tail effects, Eq. (19) of [39]; $\delta_{\ell m}$ is a residual phase correction, Eqs. (20-28) of [39]; and $\rho_{\ell m}$ is the residual amplitude correction, that we keep up to 5PN fractional accuracy [101], although their knowledge (and that of the $\delta_{\ell m}$'s) has been recently increased up to 14PN fractional order [103].

Note that the argument in the multipoles of Eq. (5) (and therefore in Eq. (3)) is $x \equiv v_\varphi^2 = (r\Omega)^2$, that is preferable to $x_{\mathrm{circ}} \equiv \Omega^{2/3}$ due to the violation of the circular Kepler's constraint during the plunge phase [23, 102]. The sum in Eq. (4) is truncated at $\ell_{\max} = 8$ included, and the system is initialized (in the
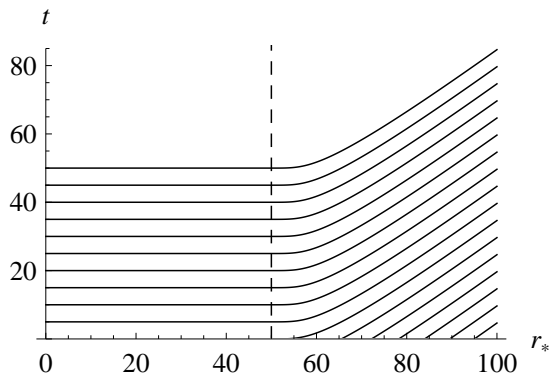
FIG. 1: Level sets of the hyperboloidal time τ as defined by Eqs. (8), (15) and (29) with respect to standard Schwarzschild coordinates $\{t, r_*\}$. The dashed line at $r_* = R_* = 50$ depicts the location of the interface between the inner domain and the hyperboloidal layer.

strong-field region $6 < r \leq 7$) with post-circular initial data [18, 30], which yields negligible initial eccentricity. The dynamics is then computed by solving Eqs. (1)-(7) of Paper I.

III. A HYPERBOLOIDAL FOLIATION OF SCHWARZSCHILD SPACETIME

In this Section we discuss the hyperboloidal layer approach in Schwarzschild spacetime. We construct a hyperboloidal foliation by gluing together a truncated Cauchy surface, which covers the strong-field region of the particle motion, and a hyperboloidal surface [81]. Because a hyperboloidal surface is spacelike by construction, and because Cauchy surfaces are also spacelike, one can choose a global hyperboloidal foliation to agree with Cauchy surfaces in a compact inner domain that includes the motion of the particle and the central black hole. This choice allows us to employ standard coordinates near the central black hole. The outer, asymptotic, domain is included in the hyperboloidal layer.

A. General properties

A hyperboloidal layer is defined as a compact radial shell in which the spacelike foliation approaches null infinity and the radial coordinate is compactified. We determine the coordinates by requiring that outgoing null surfaces have the same representation in the layer coordinates as in the inner domain coordinates. We connect the coordinates used in the compact inner domain (Cauchy region) with the coordinates used in the outer domain (hyperboloidal layer) at an interface.

We depict such a foliation with respect to standard coordinates $\{t, r_*\}$ in Fig. 1. The level sets of the new time function, $\tau(t, r_*)$, agree with the level sets of the
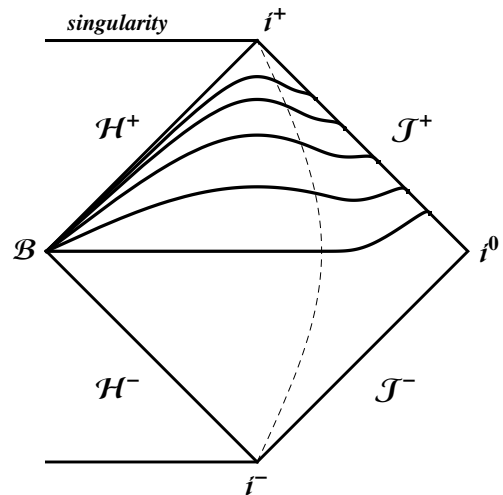

FIG. 2: Penrose diagram of Schwarzschild spacetime depicting the causal properties of the foliation plotted partially in Fig. 1. The dashed line indicates the interface to the hyperboloidal layer. The time surfaces agree with standard Schwarzschild time surfaces to the left of the interface. The diagram also shows that the foliation stays spacelike everywhere, including the asymptotic domain near null infinity.

standard Schwarzschild time, t, for $r_* \leq R_* = 50$. The dashed line indicates the timelike surface, referred to as the interface ($r_* = R_* = 50$), at which we smoothly modify the spacelike surfaces to approach outgoing null rays asymptotically.

The spacelike surfaces partially depicted in Fig. 1 approach outgoing null rays, but never become null surfaces themselves. The asymptotic causal structure can not be clearly depicted in Fig. 1. A better visualization of the causal structure is the Penrose diagram in Fig. 2. The interface (still represented by a dashed line) is depicted close to the black hole for visualization, but the causal structure is accurate in this diagram. We see that the hyperboloidal foliation agrees with standard t surfaces near the black hole. Beyond the interface, the surfaces smoothly approach future null infinity in a spacelike manner. Although the surfaces look like they are becoming null in Fig. 1, the Penrose diagram in Fig. 2 clearly shows that the surfaces are spacelike everywhere. This causal behavior allows us to solve a usual initial-boundary value problem, while extracting gravitational waveforms at future null infinity.

The hyperboloidal foliation that we employ is not only suitable for wave extraction, it also provides a solution to the outer boundary problem. Instead of truncating the simulation domain at a finite but large distance, we employ a compactifying coordinate with respect to which null infinity is at a finite coordinate location. It is well known that compactification leads to loss of resolution near the outer boundary when Cauchy foliations are used [104]. We do not run into this problem because we need to resolve only a finite number of oscillations on an infinite domain along hyperboloidal foliations, as op-
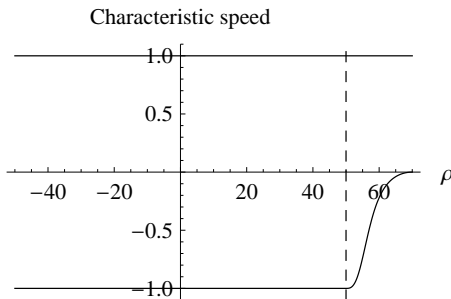
FIG. 3: Characteristic speeds on the numerical grid as given in Eq. (3). The dashed line denotes the location of the interface between the inner domain and the hyperboloidal layer. The outgoing speed has the same value in the inner domain as in the layer, whereas the incoming speed smoothy approaches zero in the layer.

posed to an infinite number of oscillations along Cauchy foliations [100].

A good illustration that compactification solves the outer boundary problem is given by a depiction of characteristic speeds on the numerical grid (Fig. 3). The outgoing speed of characteristics is nonvanishing finite at future null infinity. The incoming speed, on the other hand, vanishes because future null infinity is itself an incoming null surface (Fig. 2). No outer boundary conditions are needed because there are no incoming characteristics from the outer boundary.

Note that the compactifying coordinate is conceptually independent from the hyperboloidal foliation. We can choose any compactifying coordinate along the spacelike surfaces of our foliation compatible with scri-fixing. The choice of hyperboloidal foliation and compactification together determines the structure of characteristics on the numerical grid. The choices for Fig. 3 ensure that the outgoing characteristic speed is unity in the layer. In the next Section we discuss how to achieve this.

B. Explicit construction of the hyperboloidal layer

There are different ways to construct a hyperboloidal layer. One we find most lucid is to consider the expression of outgoing null rays in local coordinates. In standard waveform extraction methods, the solution is computed along t surfaces and the waveform is plotted along the outgoing null surfaces $t - r_*$. Naturally, we would like to keep the expression of outgoing null rays invariant in our formulation. We would also like to keep the time direction invariant, so that ringdown frequencies or decay rates that we compute are physical. Our requirements for a suitable hyperboloidal layer are as follows:

1. The exterior timelike Killing vector field in local coordinates is kept invariant in the layer.

2. The outgoing null rays in local coordinates is kept invariant in the layer.

3. The local coordinates in the layer agree with the standard $\{t, r_*\}$ coordinates at the interface.

Now we formalize these requirements. The first requirement gives a relation between the new time coordinate τ and the standard time coordinate t. The requirement that the Killing field is kept invariant translates into $\partial_t = \partial_\tau$. This condition is fulfilled by a transformation of the form

$$\tau = t - h(r_*) \,, \qquad (6)$$

where the function $h(r_*)$ is called the *height function*. The height function can only depend on spatial coordinates to leave the timelike Killing field invariant. We let the height function depend only on the tortoise coordinate because our problem is spherically symmetric.

Under the transformation (6) the Schwarzschild metric (1) becomes

$$g = A \left(-d\tau^2 - 2H d\tau dr_* + \left(1 - H^2\right) dr_*^2 \right) + r^2 d\sigma^2, \quad (7)$$

where $H \equiv dh/dr_*$ is called the *boost function*. For example, ingoing Eddington-Finkelstein coordinates are obtained with $H = -2/r$. Similarly, Painlevé-Gullstrand coordinates are obtained with $H = -\sqrt{2/r}$. The constant time hypersurfaces in these coordinates foliate the event horizon instead of intersecting at the bifurcation sphere and are therefore suitable for excision. Note that both choices give $H = -1$ at the horizon [105].

We require an analogous behavior in the asymptotic domain, in the sense that the resulting surfaces should foliate future null infinity instead of intersecting at spatial infinity. The analogy with excision indicates that one needs to satisfy $H = 1$ at infinity. The choice of a suitable boost function follows from the second item in our list. We require that the outgoing null rays in local coordinates is kept invariant. Denoting the layer coordinates with $\{\tau, \rho\}$, we require

$$t - r_* = \tau - \rho \,, \qquad (8)$$

where ρ is a yet unspecified compactifying coordinate. By combining Eqs. (6) and (8) we get for the height function $h(r_*) = r_* - \rho(r_*)$. Taking the derivative of this equation with respect to r_*, we obtain the following relation between the boost function H and the Jacobian $d\rho(r_*)/dr_*$ of the spatial compactification

$$\frac{d\rho}{dr_*} = 1 - H \,. \qquad (9)$$

The Jacobian of any compactification vanishes at the domain boundary, so we have $H = 1$ at null infinity.

The condition (8) has two important consequences. First, the outgoing characteristic speed, which is $+1$ in the inner domain, remains $+1$ also across the hyperboloidal layer. Second, the incoming characteristic speed, which is -1 in the inner domain, smoothly decreases in
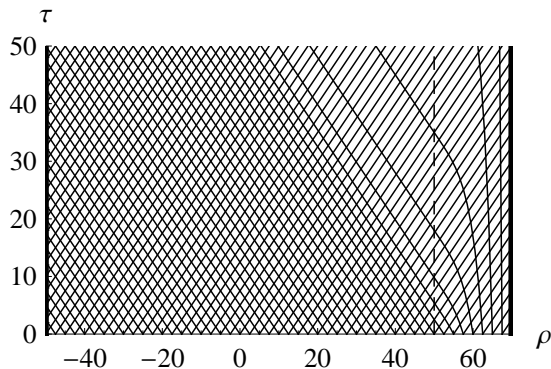
FIG. 4: The structure of the characteristics on the numerical grid. Compare Figs. 1, 2, and 3.

the layer to reach zero at future null infinity. This is easily seen by writing the Schwarzschild metric (7) using the compactifying coordinate ρ as[1]

$$g = A\left(-d\tau^2 - \frac{2H}{1-H}d\tau d\rho + \frac{1+H}{1-H}d\rho^2\right) + r(\rho)^2 d\sigma^2.$$
(10)

The outgoing (c_+) and incoming (c_-) characteristic speeds of spherically symmetric null surfaces read

$$c_+ = 1, \qquad c_- = -\frac{1-H}{1+H}.$$
(11)

Note that $c_- = 0$ at the outer boundary of the ρ-domain, where $H = 1$ by (9). The speeds are plotted in Fig. 3 for a particular choice of spatial compactification that we describe in Sec. III C.

Let us now discuss the third condition in our list, namely the requirement that the new coordinates $\{\tau, \rho\}$ agree with standard coordinates $\{t, r_*\}$ at the interface between the inner domain and the hyperboloidal layer. This condition can be fulfilled by a suitable choice of the compactifying coordinate. The spatial compactification $r_*(\rho)$ shall have the following differentiability properties along the interface at $r_* = R_*$

$$r_*(R_*) = R_*,$$
(12)

$$\left.\frac{dr_*}{d\rho}\right|_{\rho=R_*} = 1,$$
(13)

$$\left.\frac{d^k r_*}{d\rho^k}\right|_{\rho=R_*} = 0, \quad k > 1.$$
(14)

These relations imply that the coordinates r_* and ρ, and therefore t and τ, agree along the interface to kth order.

---

[1] Note that the metric in Eq. (10) is singular at the boundary because the Jacobian of any compactification is singular. This singularity can be rescaled away with a conformal factor, but such a rescaling is not necessary for our purposes because the RWZ equation in hyperboloidal compactification is regular without an explicit conformal rescaling of the background [86].

We give an explicit choice for the compactification $r_*(\rho)$ in Sec. III C.

For completeness, we finally depict in Fig. 4 the global structure of the characteristics propagating along the numerical grid $\{\tau, \rho\}$ in a suitable hyperboloidal compactification. The outgoing characteristics are straight lines with 45 degrees to the ρ-axis, just as for the $\{t, r_*\}$ coordinates. In agreement with Eq. (11) and Fig. 3, there are no incoming characteristics from the outer boundary.

A point where our approach can be further improved is indicated in Fig. 4. We truncate the infinite computational domain in r_* to the left arbitrarily at $r_* = -50$. As a result, there are incoming modes from the inner boundary that need to be set by artificial boundary conditions. This procedure can contaminate the interior solution and make the calculation of GWs absorbed by the black hole inaccurate (for example, to reduce contamination Ref. [106] uses a very large value of the extraction radius, $r_*^{\mathrm{extr}} = -1500M$, for computing the absorbed fluxes). In addition, the efficiency of the numerical computation is reduced by the coordinates used near the black hole. We accept these disadvantages because we want to describe the dynamics of the test-mass using $\{t, r_*\}$ coordinates, exactly as in Paper I.

A way to avoid the inner timelike boundary near the black-hole horizon is to work in horizon-penetrating coordinates in combination with excision. Then one needs to transform the RWZ equations, their sources, as well as the relative dynamics of the binary, that we used in Paper I, to horizon-penetrating coordinates (coordinate-independent expressions for the RWZ equations and sources are explicitly given in Ref. [92, 96]). Using a horizon-penetrating, hyperboloidal foliation is the cleanest option to compute accurately both the asymptotic and the absorbed waves. Alternatively, one can construct such coordinates also by attaching an internal layer to the truncated $\{t, r_*\}$ domain so that the event horizon, $r_* = -\infty$, is compactified. Because our main focus in this study is on the asymptotic waveform, we use the hyperboloidal layer only in the exterior asymptotic domain.

C. Spatial compactification

We present the form of the compactifying coordinate that we use in our numerical calculations. We transform r_* by introducing a compactifying coordinate ρ via

$$r_* = \frac{\rho}{\Omega(\rho)},$$
(15)

where, $\Omega(\rho)$ is a suitable function of ρ (not to be confused with the orbital frequency in Sec. II). The function $\Omega(\rho)$ has similar properties as the conformal factor in the conformal compactification of asymptotically flat spacetimes proposed by Penrose [107, 108]. For the regularity of the transformation in the interior we require that Ω has a definite sign, say, $\Omega > 0$ for all $\rho < S$, where S denotes the coordinate location of null infinity, and therefore the

zero set of Ω. To map the infinite domain $R_* \leq r_* < +\infty$ to the finite domain $R_* \leq \rho \leq S$ we require

$$\Omega(S) = 0, \quad \Omega'(S) \neq 0. \tag{16}$$

where $\Omega' \equiv d\Omega/d\rho$.

In addition, we also require that our coordinates agree with standard coordinates in an inner domain. Therefore we set $\Omega = 1$ for all $\rho \leq R_*$, where R_* denotes the location of the interface. The transition to the layer at this interface needs to be sufficiently smooth for a stable numerical implementation. We require in accordance with Eqs. (13)-(14)

$$\left.\frac{d^k\Omega}{d\rho^k}\right|_{\rho=R_*} = 0 \quad \text{with} \quad k \geq 1. \tag{17}$$

The maximum value of k for which the above property is satisfied determines the differentiability of the layer.

By differentiating Eq. (15), we get with Eq. (9)

$$H(\rho) = 1 - \frac{\Omega^2}{\Omega - \rho\,\Omega'}\,. \tag{18}$$

The form of the compactifying coordinate (15) is convenient because it allows us to control the hyperboloidal foliation by a suitable function $\Omega(\rho)$ via Eq. (18). It also makes the connection to the definition of asymptotic flatness within the Penrose conformal compactification picture clear. However, we emphasize that, in our specific case, we can also use a more general transformation than (15), which fulfills the conditions of a coordinate compactification.

IV.   THE RWZ EQUATIONS

In this Section we discuss the RWZ equations as implemented numerically. For the relations of the RWZ master function with the asymptotic observable quantities see Appendix B.

A.   The RWZ equations in the interior

In the interior domain the RWZ equations with a point-particle source are written as in Paper I. Given the dynamics of the particle, one solves the following two decoupled partial differential equations for each multipole (ℓ, m) of even (e) or odd (o) type[2]

$$\partial_t^2 \Psi_{\ell m}^{(e/o)} - \partial_{r_*}^2 \Psi_{\ell m}^{(e/o)} + V_\ell^{(e/o)} \Psi_{\ell m}^{(e/o)} = \mathcal{S}_{\ell m}^{(e/o)}, \tag{19}$$

---

[2] In our case, these correspond respectively to multipoles with $\ell + m =$ even and $\ell + m =$ odd.

with source terms $\mathcal{S}_{\ell m}^{(e/o)}$ that are explicit functions of the phase-space variables (r_*, p_*). The sources have the structure

$$\mathcal{S}_{\ell m}^{(e/o)} = G_{\ell m}^{(e/o)}(r, t)\delta(r_* - r_*(t))$$
$$+ F_{\ell m}^{(e/o)}(r, t)\partial_{r_*}\delta(r_* - r_*(t))\,, \tag{20}$$

where $r_*(t)$ is here indicating the particle radial coordinate. The explicit expressions for the sources are given in Eqs. (20)-(21) of [18], to which we address the reader for further technical details. In our approach the distributional δ-function is approximated by a narrow Gaussian of finite width $\sigma \ll M$ (see Sec. V B).

B.   The RWZ equations in the hyperboloidal layer

As explained in Sec. III there are three essential steps to the construction of the hyperboloidal layer:

1. Introduce a new time coordinate τ, Eq. (6), that preserves the stationarity of the background,

$$\partial_t = \partial_\tau \quad \Rightarrow \quad \tau = t - h\,. \tag{21}$$

2. Fix the time coordinate such that the expression of the outgoing null rays is invariant in the layer,

$$t - r_* = \tau - \rho \quad \Rightarrow \quad H = 1 - \frac{d\rho}{dr_*}\,. \tag{22}$$

3. Choose a suitable compactifying coordinate ρ so that the coordinates in the layer agree with the coordinates near the black hole, satisfying the conditions (12)-(14).

The whole prescription results in is a simple coordinate transformation, $\{t, r_*\} \to \{\tau, \rho\}$, that satisfies the above properties. The derivative operators in standard coordinates transform as

$$\partial_t = \partial_\tau, \qquad \partial_{r_*} = -H\,\partial_\tau + (1 - H)\,\partial_\rho\,. \tag{23}$$

Applying this transformation on Eq. (19) (dropping all multipolar indices)

$$(\partial_t^2 - \partial_{r_*}^2 + V)\Psi = \mathcal{S}, \tag{24}$$

we get for the wave operator in the new coordinates

$$\partial_t^2 - \partial_{r_*}^2 = -(1 - H^2)\partial_\tau^2 +$$
$$+(1 - H)\left(-2H\partial_\tau\partial_\rho + (1 - H)\partial_\rho^2 - (\partial_\rho H)(\partial_\tau + \partial_\rho)\right).$$

We can take out a $(1 - H)$ term from the operator. We need to be careful with the lower order terms in (24). The source term is compactly supported in a neighborhood of the particle in the interior domain and therefore is not a concern. The potential, however, is nonvanishing in the wave zone. Its fall-off behavior is essential for the applicability of the hyperboloidal method [86]. The

potential in the RWZ equation falls off as r^{-2} both for even and odd parity perturbations. Therefore we can introduce the rescaled potential

$$\bar{V} \equiv V/(1 - H), \qquad (25)$$

which has a regular limit at null infinity. To see this, consider for example the odd-parity (Regge-Wheeler) potential

$$V^{(\mathrm{o})} = \frac{1}{r^2} \left(\ell(\ell + 1) - \frac{6}{r} \right) , \qquad (26)$$

we have with (18)

$$\bar{V}^{(\mathrm{o})} = \frac{V^{(\mathrm{o})}}{1 - H} = \frac{(\Omega - \rho\,\Omega')}{\rho_r^2} \left(\ell(\ell + 1) - \frac{6\Omega}{\rho_r} \right) , \quad (27)$$

where $\rho_r \equiv \Omega\, r$. The rescaled Schwarzschild radius ρ_r has a nonvanishing limit at infinity because r and r_* coincide asymptotically. As a result, we have $\rho_r = \rho = S$ at infinity. An analogue regular expression holds also for the even-parity (Zerilli) potential.

Then we can write the RWZ equation in the layer as

$$-(1 + H)\partial_\tau^2 \Psi - 2H\partial_\tau\partial_\rho \Psi + (1 - H)\partial_\rho^2 \Psi$$
$$-(\partial_\rho H)(\partial_\tau + \partial_\rho)\Psi + \bar{V}\Psi = 0. \qquad (28)$$

From this form of the equation, it is immediately clear that setting $H = 0$ recovers the standard RWZ equation (19). We also see that the equation is regular and pure outflow at infinity ($H = 1$).

V. NUMERICS

The numerical technique employed in our code is a standard combination of finite-difference approximation for the spatial derivatives and Runge-Kutta methods for time integration [10, 86]. In this section we briefly review the method.

A. Numerical methods

Our code solves the RWZ equation in first-order-in-time second-order-in-space form adopting the method of lines and the Runge-Kutta 4th order scheme. The right hand side is discretized in space on a uniform grid in the coordinate $\rho \in [\rho_{\min}, S]_{R_*}$, where R_* denotes the interface to the hyperboloidal layer and S the coordinate location of $\mathscr{I}^+$. Finite differences are employed for the derivatives. We use 4th order central stencils in the bulk, lop-sided or sided 4th order stencils for the outermost points ($\rho = \rho_{\min}$ and $\rho = S$). No boundary data is prescribed at $\mathscr{I}^+$, whereas maximally dissipative 4th order convergent outgoing boundary conditions [109] are imposed at the inner boundary. Kreiss-Oliger type dissipation is added to the RWZ equation. The particle

trajectory is updated using a 4th order Runge-Kutta integrator with adaptive time-step. The convergence of the code is demonstrated in Appendix A.

In our numerical computations we set

$$\Omega = 1 - \left(\frac{\rho - R_*}{S - R_*} \right)^4 \Theta(\rho - R_*), \qquad (29)$$

though various other choices are possible. The step function, $\Theta(\rho - R_*)$, indicates that compactification is performed only for $\rho > R_*$. We choose the numerical domain as $[\rho_{\min}, S]_{R_*} = [-50, 70]_{50}$; Figs. 1, 3, and 4 refer to these settings. For the production runs that we present below, the ρ-domain is covered by 12001 points, that correspond to gridspacing $\Delta\rho = 0.01$.

B. Particle treatment

Following previous work [10, 18], the δ-function in the RWZ source is represented by a narrow Gaussian of finite width $\Delta\rho < \sigma \ll M$. The hyperboloidal compactification has an advantage also on the treatment of the Dirac distribution via a smooth Gaussian because most of the computational resources are used for the strong-field, bulk region so that narrow Gaussians can be efficiently resolved. For the production runs that we present below, we use $\sigma = 0.08M$.

We inject zero initial data for the RWZ master functions switching on the sources progressively in time [3] following the prescription [110],

$$S \mapsto \frac{S}{\exp\left[-a_0(t - t_0)\right] + 1} , \qquad (30)$$

where typically $a_0 = 1/M$ and $t_0 = 40\,M$. We observed that this smooth switch-on significantly reduces the (localized) "junk" radiation contained in the initial data, without, obviously, eliminating it completely.

VI. RESULTS

Let us briefly summarize our main results. In Sec. VI A we focus on circular orbits to assess the performance of our new numerical implementation. We compute the gravitational energy flux emitted at null infinity by a particle on stable circular orbits and compare it with the semi-analytic data of Fujita et al. [113]. We also compute (and characterize) the GW energy flux emitted by the particle on unstable circular orbits. In particular, we extract from the data the corresponding residual amplitude corrections $\rho_{\ell m}$ introduced in Ref. [39]. We focus then on the transition from quasi-circular inspiral

---

[3] This approach has been suggested to reduce the impact of Jost solutions [110–112].
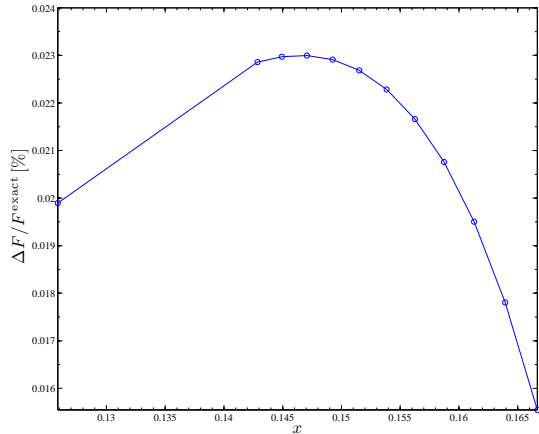
FIG. 5: Stable circular orbits: fractional difference between the RWZ total energy flux computed with our code and extracted at $\mathscr{I}^+$ (up to $\ell = 8$) and the corresponding semi-analytic data computed by Fujita et al. [113].
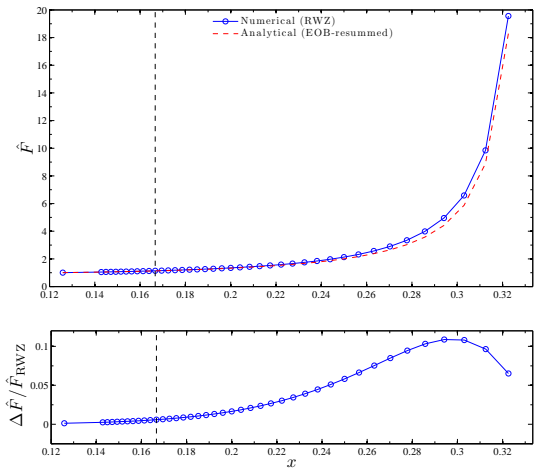

FIG. 6: Newton-normalized total gravitational wave energy flux summed up to $\ell = 8$. The analytical (5PN-accurate, EOB-resummed) flux is compared with the numerical points, that include also unstable circular orbits. The vertical dashed line indicates the LSO location at $x = 1/6$.

to plunge, merger and ringdown. In Sec. VI B we discuss the total gravitational waveform, including up to $\ell_{\max} = 8$ multipoles, extracted at $\mathscr{I}^+$. This waveform is then compared in Sec. VI B 1 to waveforms extracted at finite radii. We estimate phase and amplitude differences and test the standard extrapolation procedure that is routinely applied to NR waveforms. In Sec. VI C a self-consistency check of the treatment of the dynamics is presented. Our prescription for the radiation reaction is checked on consistency (even beyond the LSO crossing) between the GW angular momentum flux extracted at $\mathscr{I}^+$ and the (5PN EOB-resummed) mechanical angular momentum loss $\mathcal{F}_\varphi$. In Sec. VI D we compute the final and maximum gravitational recoil of the final black-hole in the $\nu \to 0$ limit, obtaining a more accurate estimate than the ones given in Paper I.

A. Circular orbits

1. Accuracy: comparison with data by Fujita et al.

As a test of the accuracy of our new setup we compute the gravitational wave energy and angular momentum fluxes emitted by a particle on stable circular orbits. For each orbital radius, r_0 (in units of M hereafter), we consider the complete multipolar waveform (up to $\ell_{\max} = 8$) measured at $\mathscr{I}^+$ and compute the fluxes summing together all multipoles via Eqs. (B2) and (B3). We consider circular orbits belonging to both the stable branch ($r_0 \geq 6$) and the unstable branch ($3 < r_0 < 6$). The computation of the GW fluxes from stable circular orbits in Schwarzschild spacetime has been performed several times in the past, with different integration techniques (either in time domain or in frequency domain) and with

increasing level of accuracy [106, 113–117]. Currently, the method that yields the most accurate results is the one developed by Fujita et al. [113], which allows for the computation of emitted fluxes with a relative error of order 10^{-14}. We checked the accuracy of our numerical setup (finite differencing with a hyperboloidal layer and wave extraction at $\mathscr{I}^+$) by considering a small sample of stable orbits, with radii in the range $6 \leq r_0 \leq 7.9456$ and spaced by $\Delta r_0 = 0.1$ for $6 \leq r_0 \leq 7$. The full multipolar information for $r_0 = 7.9456$ (both energy and angular momentum fluxes) is listed in Table II in Appendix A, so to facilitate the comparison with published data [106, 114]. In addition, a direct comparison with the data kindly given to us by Ryuichi Fujita and computed as in Ref. [113], that we consider "exact", reveals that our finite-differencing, time-domain computation is rather accurate: The relative difference $\Delta F_{\ell m}/F_{\ell m}^{\text{Exact}} = (F_{\ell m}^{\text{RWZ}} - F_{\ell m}^{\text{Exact}})/F_{\ell m}^{\text{Exact}}$ in energy flux is below 0.8 % in almost every multipolar channel (see Appendix A for more detailed information). Summing together all multipoles, we find that the total energy flux, dominated by the modes with smaller values of ℓ and with $m = \ell$, agrees with the exact data within 0.02 %. In Fig. 5 we show the relative difference between total fluxes, $\Delta F/F^{\text{Exact}} = (F^{\text{RWZ}} - F^{\text{Exact}})/F^{\text{Exact}}$ (summed up to $\ell_{\max} = 8$), versus $x = 1/r_0$.

2. Total energy flux, unstable orbits and the "exact" multipolar amplitudes $\rho_{\ell m}$

Now that we have assessed the accuracy of our finite-difference, time-domain code, we calculate the GW en-
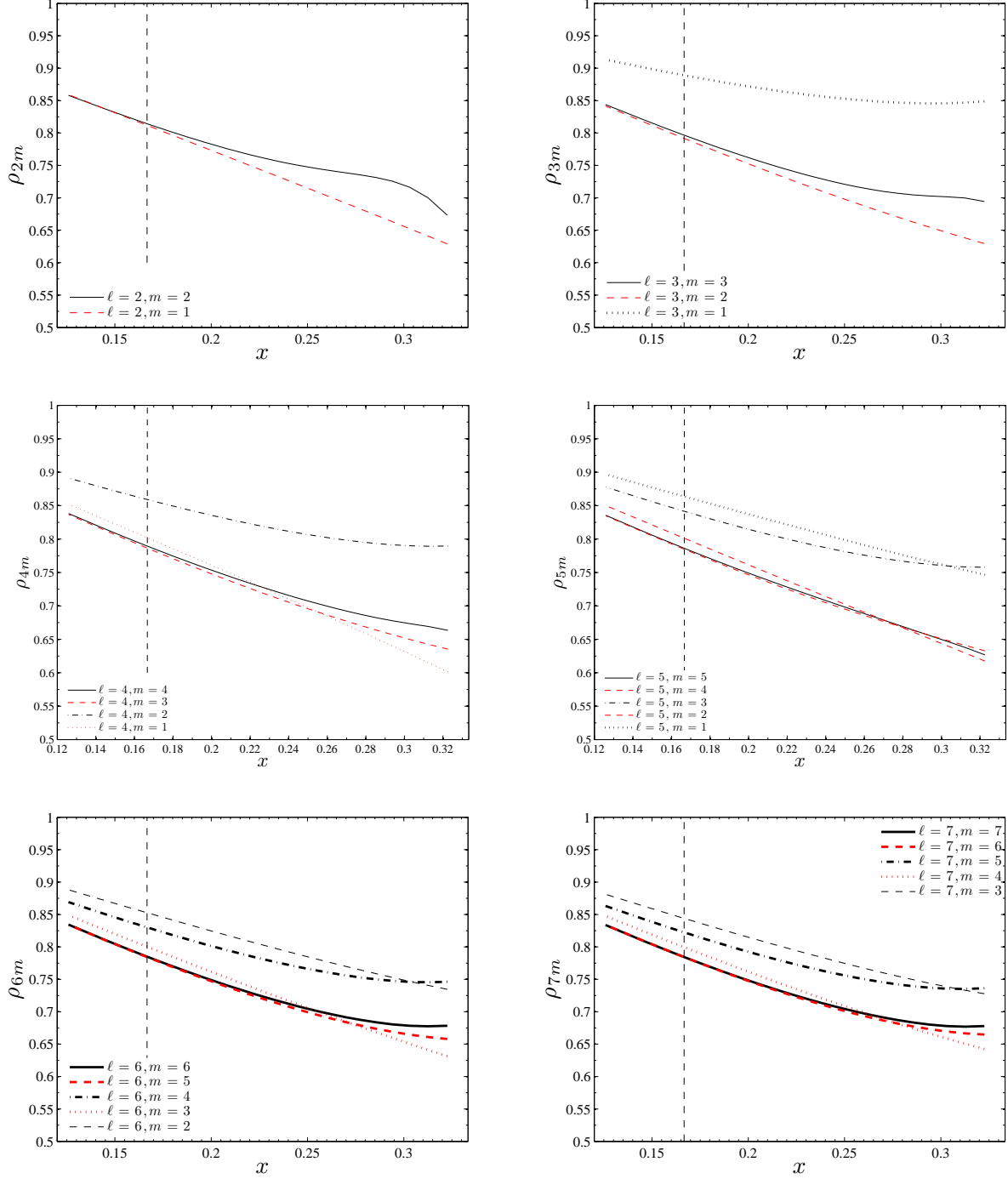
FIG. 7: The "exact" functions $\rho_{\ell m}$ extracted from the numerical fluxes for $1/7.9456 \leq x \leq 1/3.1$. The vertical dashed line indicates the LSO location, $x = 1/6$.

ergy flux for *unstable* circular orbits, i.e. orbits with radii in the range $3 < r_0 < 6$. This computation has received a rather poor attention in the literature. To our knowledge, the only computation along unstable orbits was performed in Ref. [39] for the $\ell = m = 2$ flux and with less good accuracy than what we are able to do here. In [39] it was pointed out that the knowledge of

the emitted flux also *below* the LSO might be helpful to improve the resummation of the residual amplitude corrections $\rho_{\ell m}$ that enter the factorized (EOB-resummed) multipolar waveform introduced there.

We compute the multipolar fluxes for a sample of unstable circular orbits with $3.1 \leq r_0 < 6$, spaced by $\Delta r_0 = 0.1$. Figure 6 shows in the top panel (as a solid

line with circles) the two branches together, both for stable and unstable orbits, of the Newton-normalized total energy flux, $\hat{F} = F_{\ell m}/F_{22}^N$, summed over all multipoles up to $\ell_{\max} = 8$. The vertical dashed line indicates the location of the LSO at $x = 1/6$.

It is interesting to ask how reliable is the 5PN-accurate EOB-resummed analytical representation of the flux over the sequence of unstable orbits. We recall that Ref. [39] introduced a specific factorization and resummation of the PN waveform such that the related analytical flux was found to agree very well with the numerical one (see Fig. 1 (d) of [39]). For this reason the top panel of Fig. 6 additionally shows the energy flux constructed analytically from the resummed circularized multipolar waveform of [39] that includes all the 5PN-accurate terms computed in [101]. The relative difference between fluxes is plotted in the bottom panel. The figure indicates a remarkable agreement between the analytical and numerical fluxes also for circular orbits *below* the LSO, with a relative difference that is almost always below 5%. Note that the difference becomes as large as 10% only for the last 6-7 orbits, which are very close to the light ring ($x = 1/3$). It is, however, remarkable that the analytical expression for the flux, based on suitably resummed 5PN-accurate (only) results remains rather reliable in a region were the velocity of the orbiting particle is about half the speed of light. It will be interesting in the future to perform such a comparison with the 14PN-accurate expression of the waveform recently computed analytically by Fujita [103].

In the spirit of the factorized form of the multipolar waveform entering the analytical flux, Eqs. (4)-(5), the most important information one wants to extract from the numerical data is the behavior of the residual amplitudes $\rho_{\ell m}^{\text{Exact}}(x)$ also along unstable orbits. These quantities are the real unknowns of the problem, since all other factors, i.e. the source $S^{(\epsilon)}(x)$ and the tail factor $T_{\ell m}(x)$, are known analytically. In this respect, the complete knowledge of the $\rho_{\ell m}^{\text{Exact}}$'s brings in the full strong-field information that is only partially available via their PN expansion The computation of $\rho_{\ell m}^{\text{Exact}}$ was performed for the first time in Ref. [39]. It was restricted mainly to stable orbits, with multipoles up to $\ell_{\max} = 6$, and was based on the numerical data computed by Emanuele Berti [116, 117]. In addition, as mentioned above, a small sample of unstable orbits were also considered to explore the behavior of ρ_{22}^{Exact} toward the light ring.

The exact $\rho_{\ell m}^{\text{Exact}}$ are obtained from the partial fluxes $F_{\ell m}^{\text{Exact}}$ as

$$\rho_{\ell m}^{\text{Exact},(\epsilon)}(x) = \left\{ \frac{\sqrt{F_{\ell m}^{\text{Exact}}/F_{\ell m}^{\text{Newton}}}}{|T_{\ell m}|\hat{S}^{(\epsilon)}} \right\}^{1/\ell} \tag{31}$$

where the source $S^{(\epsilon)}$ is either the energy (for even-parity multipoles, $\epsilon = 0$), or the Newton-normalized angular momentum (for odd-parity multipoles, $\epsilon = 1$) along cir-
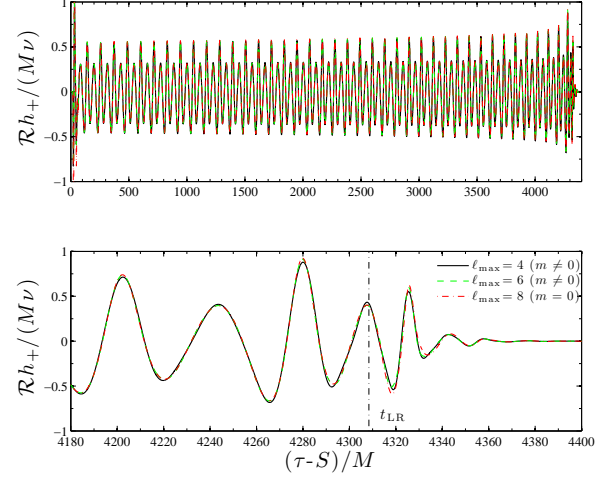

FIG. 8: (Color online). The $\mathcal{R}h_+/(M\nu)$ polarization (from Eq. (B1)) of the gravitational waveform for $\nu = 10^{-3}$. The top panel shows the complete wave train (~ 40 orbits up to merger). The bottom panel focuses around the merger time and illustrates the impact of subdominant multipoles. The vertical dashed line indicates the light-ring crossing time by the point-particle.

cular orbits, i.e.

$$\hat{S}^{(0)}(x) = \frac{1 - 2x}{\sqrt{1 - 3x}} \tag{32}$$

$$\hat{S}^{(1)}(x) = \frac{1}{\sqrt{1 - 3x}}. \tag{33}$$

The square modulus of the tail factor $T_{\ell m}$ reads [23, 39]

$$|T_{\ell m}|^2 = \frac{1}{(\ell!)^2} \frac{4\pi\hat{\hat{k}}}{1 - e^{-4\pi\hat{\hat{k}}}} \prod_{s=1}^{\ell} \left[s^2 + \left(2\hat{\hat{k}}\right)^2 \right] \tag{34}$$

where $\hat{\hat{k}} = mx^{3/2}$.

The result of the computation is presented in Fig. 7 including multipoles up to $\ell_{\max} = 7$. The figure clearly shows that, for some multipoles, the quasi-linear behavior of the $\rho_{\ell m}(x)$ above the LSO (explained in detail in [39]) is replaced by a more complicated shape below the LSO, where high-order corrections seem relevant. The figure completes below the LSO the data of Fig. 3 of [39], where only stable orbits were considered. Indeed, in the stable branch, the curves presented here perfectly overlap with those of [39].

We postpone to future work the analytical understanding of the behavior of the various ρ_{lm}^{Exact} when $x \to 1/3$. On the basis of the analytical information already contained in Fig. 5 of Ref. [39], it seems unlikely that the current 5PN-accurate analytical knowledge of the $\rho_{\ell m}(x)$ functions can by itself explain the structure of the ρ_{lm}^{Exact} close to the light-ring. It will be interesting to see whether this structure can be fully accounted for by the 14PN-accurate results of Ref. [103].

B. Gravitational radiation from inspiral, plunge, merger and ringdown

Now we discuss the properties of the gravitational wave signal emitted by the five binaries with $\nu = 10^{-2,-3,-4,-5,-6}$. The initial relative separation is $r_0 = 7$ for $\nu = 10^{-2,-3,-4}$, $r_0 = 6.3$ for $\nu = 10^{-5}$ and $r_0 = 6.1$ for $\nu = 10^{-6}$. These latter values are chosen so that the evolution time is approximately equally long for $\nu = 10^{-4,-5,-6}$ (~ 400 inspiral orbits, see Table I). The relative dynamics is started using post-circular initial data as described in [18, 30], assuring a negligible initial amount of eccentricity. The system is then driven by radiation reaction, Eq. (3), into a (long) quasi-adiabatic inspiral, which is then smoothly followed by the nonadiabatic plunge phase, which terminates with the merger of the two bodies and the final ringdown. The relative dynamics and the multipolar structure of the waveforms are qualitatively the same as described in Paper I and II.

Let us discuss the mass ratio $\nu = 10^{-3}$ as case study. We counted about 40 orbits up to merger[4], defined as the time at which the particle crosses the light-ring ($r = 3$). Figure 8 (displayed also in Paper II and Ref. [9]) shows the $\mathcal{R}h_+/(M\nu)$ polarization, Eq. (B1), of the gravitational waveform for this binary along the fiducial direction $(\theta, \varphi) = (\pi/4, 0)$ for various multipolar approximation. The waveforms are displayed versus retarded time at $\mathscr{I}^+$, $\tau - S$. The most accurate waveform includes the multipoles up to $\ell_{\max} = 8$ (dash-dotted line). Summing up to $\ell_{\max} = 4$ captures most of the behavior up to the light ring crossing (t_{LR}, vertical dashed line), while the higher multipoles are more relevant during the late-plunge phase and ringdown. Note also the importance of the $m = 0$ modes during the ringdown.

1. Comparing waves extracted at $\mathscr{I}^+$ and at finite radii

Access to the radiation at $\mathscr{I}^+$ enables us to evaluate finite distance effects in the waveform phase and amplitude. We work again with mass ratio $\nu = 10^{-3}$ only and compare waves extracted at $\mathscr{I}^+$ with those extracted at three large, but finite, extraction radii $r_*^{\mathrm{extr}}/M = (250, 500, 1000)$. Figure 9 displays the phase differences $\Delta\phi_{\ell m} \equiv \phi_{\ell m}^{\mathscr{I}^+} - \phi_{\ell m}^{r_*^{\mathrm{extr}}}$ (left panels) and the fractional amplitude difference $\Delta A_{\ell m}/A_{\ell m} \equiv (A_{\ell m}^{\mathscr{I}^+} - A_{\ell m}^{r_*^{\mathrm{extr}}})/A_{\ell m}^{\mathscr{I}^+}$ (right panels) for the most relevant multipoles. On average, the phase differences accumulated between waves at $r_*^{\mathrm{extr}}/M = 250$ and at $\mathscr{I}^+$ is $\Delta\phi_{\ell m} \sim 0.125 - 0.25$ rad,

which decreases to $\Delta\phi_{\ell m} \sim 0.05$ rad when $r_*^{\mathrm{extr}}/M = 1000$. The corresponding fractional variation of the amplitude is $\Delta A_{\ell m}/A_{\ell m} \sim 0.2\%$ for $r_*^{\mathrm{extr}}/M = 250$, which drops down by roughly a factor of 10 for $r_*^{\mathrm{extr}}/M = 1000$. The phase differences shown in Fig. 9 are *significant*, in that they are much larger than the numerical uncertainty ($\delta\phi \sim 10^{-6}$; see convergence results in Appendix A).

An interesting feature that is common to both the phase difference and the fractional amplitude difference is that their variation is rather small during the inspiral, then decreases abruptly during the plunge (the LSO crossing is at $t_{LSO} = u = 4076.1$ for this binary) and the smallest values are reached during the ringdown. The multipolar behavior of Fig. 9 carries over to the total gravitational waveform. Figure 10 shows the phase difference between the total polarization $\mathcal{R}h_+/(M\nu)$ extracted at $\mathscr{I}^+$ and at finite radii. The phase difference amounts to (on average) $\Delta\phi \sim 0.125$ rad for $r_*^{\mathrm{extr}}/M = 250$ and $\Delta\phi \sim 0.025$ rad for $r_*^{\mathrm{extr}}/M = 1000$. Note that the modulation in the phase difference is *not* numerical noise, but it is an actual physical feature due to the combination of the (different) dephasings of the various multipoles.

We finally note that our $\ell = m = 2$ EMR results are consistent with the corresponding equal-mass results displayed in Fig. 10 of Ref. [118], where they compare the extrapolated waveform to the one extracted at $r^{\mathrm{extr}}/M = 225$. After applying both a time and a phase shift to the finite-radius waveform, they found that the accumulated phase difference to the extrapolated waveform is of order 0.2 rad, i.e. about two times our (average) dephasing for the $r_*^{\mathrm{extr}}/M = 250$ waveform.

2. Extrapolating finite-radius waveforms to $r \to \infty$

Now that we have shown that finite-radius effects are significant, we use the data at $\mathscr{I}^+$ to test, in a well controllable setup, the standard extrapolation to $r \to \infty$ routinely applied to NR finite-radius waveforms.

Indicating with r the radius at which radiation is measured in NR simulations, the waveforms are extrapolated to $r \to \infty$ by assuming an expansion in powers of $1/r$ (see e.g. Refs. [47, 48, 50, 118]),

$$f(u, r) = \sum_{k=0}^{K} \frac{f_k(u)}{r^k} , \qquad (35)$$

where f can be either the amplitude or the phase of the gravitational waveform[5]. The extrapolation procedure of NR data is affected by the fictitious identification of a background (Schwarzschild or Kerr) in the numerically generated spacetime and by subtleties in the definition of the retarded time for each observer (see e.g. Sec. IIB

---

[4] With a slight abuse of definition, we consider the number of "orbits" as the value of the orbital phase at the end of the dynamical evolution divided by 2π. In doing so we are also including in the computation the plunge phase, where the dynamics is nonadiabatic and cannot be approximated by a sequence of circular orbits.

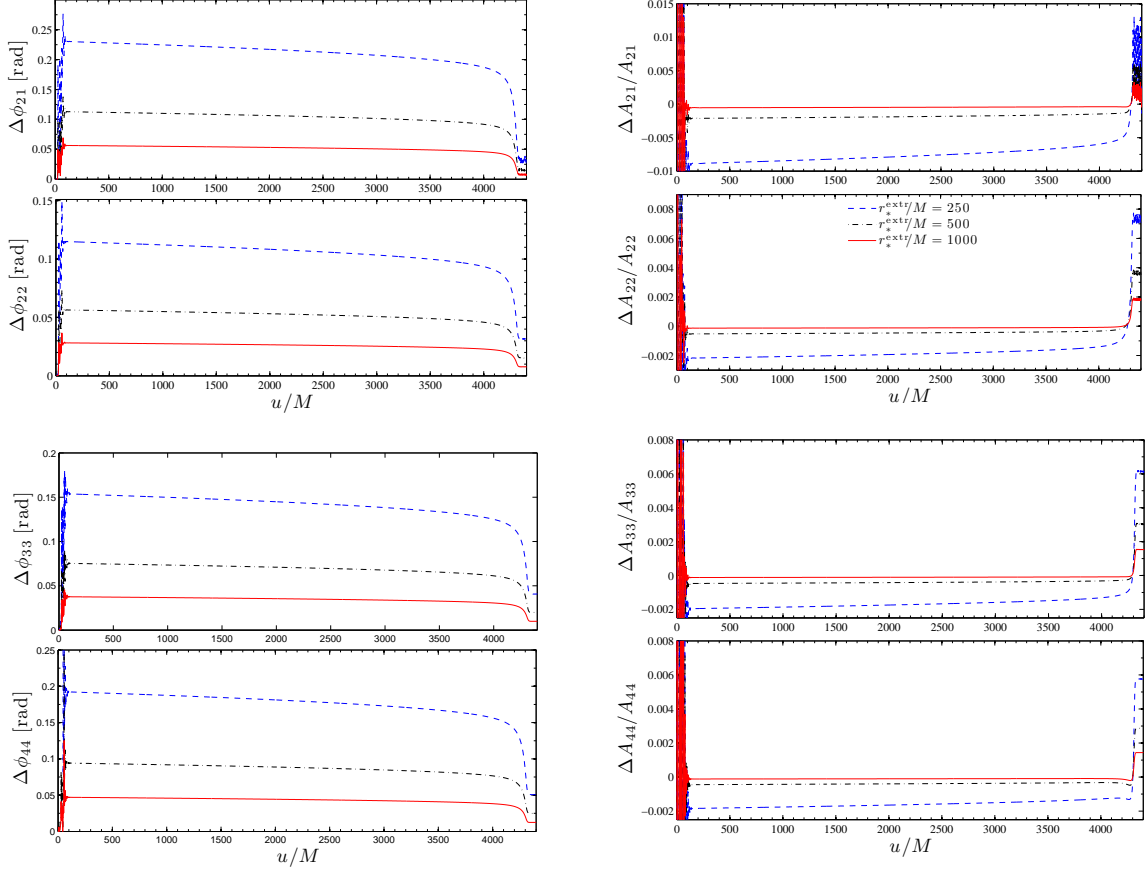[5] In NR studies the extrapolation is usually applied to the curvature waveform $r\,\psi_4$.

FIG. 9: (Color online) Phase difference (left panels) and relative amplitude difference (right panels) between multipoles extracted at $\mathscr{I}^+$ and at finite radii. Extraction radii are $r_*^{\mathrm{extr}}/M = (250, 500, 1000)$. Data refer to the $\nu = 10^{-3}$ binary.
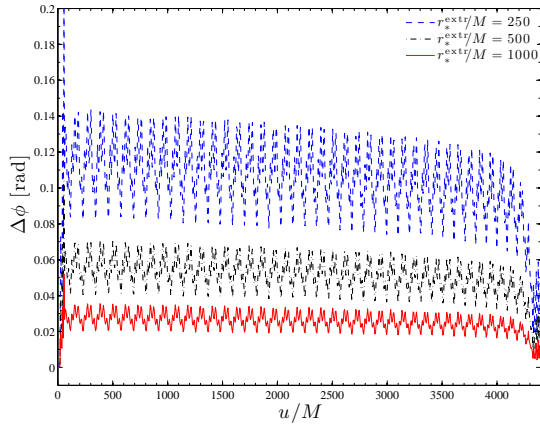

FIG. 10: (Color online) Phase difference between the $\mathcal{R}h_+/(M\nu)$ total gravitational wave polarization at $\mathscr{I}^+$ and at finite radii. Data refer to the $\nu = 10^{-3}$ binary.

of Ref. [48] and Sec. IIIC of Ref. [118]). Thanks to the aforementioned CCE procedure to compute the GW signal at $\mathscr{I}^+$, Ref. [55] was able to provide an independent

check of the extrapolation procedure. Reference [55] focused on the $\ell = m = 2$ ψ_4 waveform from an equal-mass black-hole binary and considered data extracted at $r/M = (280, 300, 400, 500, 600, 1000)$ as input for the extrapolation procedure. Over the $1000M$ of evolution from early inspiral to ringdown, Ref. [55] found a dephasing of 0.019 rad and a maximum fractional amplitude difference of 1.08% between the extrapolated and the $\mathscr{I}^+$ waveforms.

Our setup permits the validation of the expansion in Eq. (35) and a quantification of the extrapolation errors in the absence of ambiguities related to the definition of the extraction spheres and retarded times on a dynamical spacetime. The radius, r, is the areal radius of the Schwarzschild background and the retarded time is by construction $u = \tau - \rho$. To produce a meaningful comparison with the estimates of [55], we use waveforms extracted at $r_*^{\mathrm{extr}}/M = (250, 500, 750, 1000)$ as input for the extrapolation procedure, and we work again with the $\nu = 10^{-3}$ binary.

The phase and amplitude differences are plotted in Fig. 11, where we show only $\ell = 2$ multipoles for definitess (the picture does not change for other multipoles): $m = 1$ (left panel) and $m = 2$ (right panel). Different
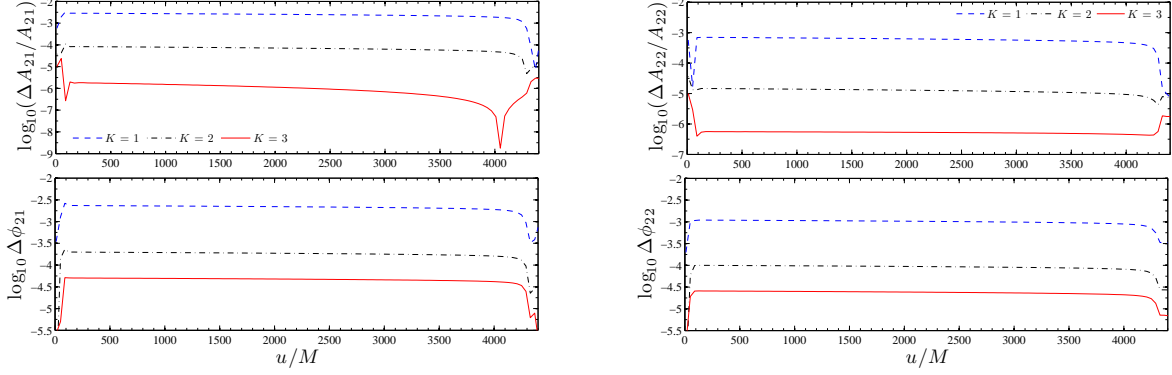
FIG. 11: (Color online). Fractional amplitude difference (top panels) and dephasing (bottom panel) between $\mathscr{I}^+$ and extrapolated waveforms. Note that we plot the $\log_{10}$. Multipoles are $\ell = m = 2$ (left panels) and $\ell = 2$, $m = 1$ (right panels). Extraction radii are $r_*/M \simeq (250, 500, 750, 1000)$. Different lines refer to different polynomial order in the extrapolation i.e. K in Eq. (35). The plot refers to the $\nu = 10^{-3}$ binary.

lines in the plot correspond to different choices of the maximum power K in the polynomial expansion (35). The phase difference between the wave at $\mathscr{I}^+$ and the extrapolated one decreases uniformly in time: It is between 10^{-2} and 10^{-3} rad when a linear polynomial ($K = 1$) in $1/r$ is assumed in Eq. (35) and it drops to between 10^{-4} and 10^{-5} when a cubic polynomial is used ($K = 3$). In this analysis we considered only up to $K = 3$ because this value seems to give the best compromise between noise and accuracy when extrapolating NR waveforms [50, 118]. We remark, however, that in our setup we are not limited in the choice of K. This is evident in Fig. 12 where we use higher values of K and more extraction radii $r_*^{\text{extr}}/M = (250, 500, 750, 1000, 2000, 4000)$, for the $\ell = m = 2$ waveform. Both the phase and amplitude differences decrease monotonically with increasing K, showing that more powers in the expansion (35) lead to more accurate extrapolation. The simple extrapolation formula (35) proves robust and leads to reliable waveforms.

C. Angular momentum loss

The main uncertainty in our approach lies, as discussed above, on the accuracy of the analytically resummed radiation reaction, Eq. (3). Several studies [10, 23] have shown the *consistency* between the gravitational wave angular momentum flux computed from the RWZ waveform (measured at a large, finite radius) and the mechanical angular momentum loss $-\hat{\mathcal{F}}_\varphi$ obtained by suitably resumming (a la Padé) the Taylor-expanded PN flux [23], or via the multiplicative decomposition of the waveform of [23, 39, 101], as performed in [10]. In particular, Ref. [10] pointed out a fractional difference between mechanical and GW angular momentum fluxes at the 10^{-3} level up to (and even below) the adiabatic LSO crossing.
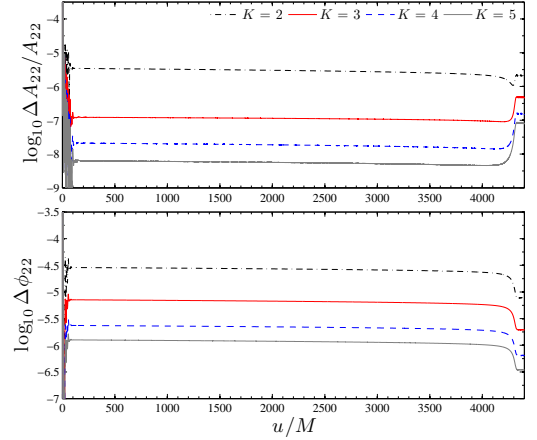

FIG. 12: (Color online). Residual of amplitude (top) and phase (bottom) between the $\mathscr{I}^+$ and the extrapolated $\ell = m = 2$ waveform. Note that we plot the $\log_{10}$. Extraction radii are $r_*^{\text{extr}}/M = (250, 500, 750, 1000, 2000, 4000)$. Different lines refer to different polynomial order in the extrapolation i.e. different K in Eq. (35). Data refer to $\nu = 10^{-3}$ binary.

The common drawback of these studies is that the target "exact" flux is computed at a finite extraction radius (typically $r_*/M = 1000$), whereas the analytical $\mathcal{F}_\varphi$ is computed (by construction) at $\mathscr{I}^+$. Because we can compute the RWZ flux at $\mathscr{I}^+$, the comparison between the instantaneous GW angular momentum flux $\dot{J}_{\text{GW}}/\nu^2$ and the mechanical angular momentum loss $\dot{J}_M/\nu^2 = -\mathcal{F}_\varphi/\nu$ is more meaningful, and can be calculated without the ambiguity caused by a relative time-shift that one should include when $\dot{J}/\nu^2$ is computed at a finite radius (it was not included in [10] for simplicity).
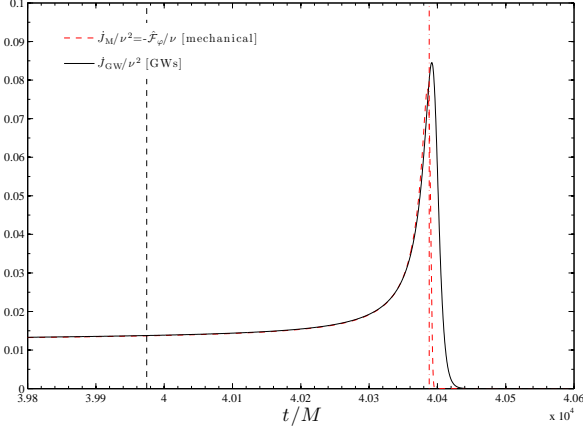
FIG. 13: (Color online). Late-time comparison between two angular momentum losses for the binary with $\nu = 10^{-4}$. The GW flux ($\dot{J}_{\rm GW}/\nu^2$, solid line) computed from the RWZ waveform and extracted at $\mathscr{I}^+$ (including up to $\ell_{\rm max} = 8$ radiation multipoles) is contrasted with the EOB-resummed, analytical mechanical angular momentum loss $-\hat{\mathcal{F}}/\nu$ (dashed line). The two vertical lines correspond (from left to right) to the particle crossing respectively, the adiabatic LSO location ($r = 6$, $t_{\rm LSO} = 39974.40$), and the light-ring location ($r = 3$, $t_{\rm LR} = 40388$).
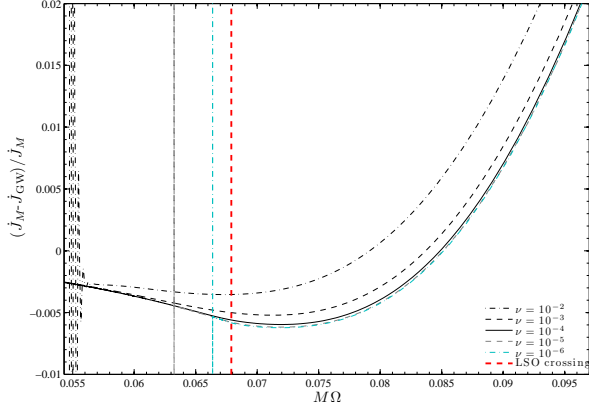

FIG. 14: (Color online). Relative difference between the mechanical angular momentum loss and the GW energy flux for the five mass ratios considered. The figure highlights how a very small fractional difference is maintained also after the LSO crossing.

We focus first on the $\nu = 10^{-4}$ simulation. In Fig. 13 we compare the mechanical angular momentum loss (changed sign, $-\hat{\mathcal{F}}_\varphi/\nu$, dashed line) to the instantaneous angular momentum flux ($\dot{J}_{\rm GW}/\nu^2$, solid line) extracted at $\mathscr{I}^+$ and plotted versus the corresponding retarded time $\tau - S$. Since $\hat{F}_\varphi$ is parametrized by the mechanical time t, we use this as x-axis label. The two vertical lines on the figure indicate (from left to right) the

particle crossing of the adiabatic LSO location ($r/M = 6$, $t_{\rm LSO} = 39974.40$, dashed black line), which can be considered approximately as the end of the inspiral, and the light-ring crossing ($r/M = 3$, $t_{\rm LR} = 40388$, dashed red line). Consistently with the findings of Paper I (compare Fig. 8 in Paper I, which used the flux at $r_*^{\rm extr}/M = 1000$), the figures confirm visually the good agreement between the two fluxes also below the LSO crossing, and actually almost during the entire plunge phase. The relatively large difference between the fluxes around the light-ring crossing is due to the lack of next-to-quasi-circular (NQC) corrections in the waveform amplitude as well as of ringdown quasi-normal-modes, in the analytically constructed $\dot{J}_M/\nu^2$. Note that Paper II has explicitly shown how these corrections can be effectively added to the "bare" inspiral resummed multipolar waveform that we use to compute radiation reaction to obtain a much closer agreement between the waveform moduli in the strong-field-fast-velocity regime. We work with NQC-free radiation reaction because the late part of the dynamics (and waveform) is practically unaffected by details of the radiation reaction, as discussed in [23].

The qualitative agreement seen in Fig. 13 is depicted more accurately in Fig. 14. The figure displays (for the five mass ratios considered) the relative difference $(\dot{J}_M - \dot{J}_{\rm GW})/\dot{J}_M$ versus the orbital frequency $M\Omega$. For reference, the LSO crossing frequency, $M\Omega_{\rm LSO} \approx 0.068$, is marked by a vertical dashed line (red online) in the figure[6]. For $\nu = 10^{-3}$, the relative difference is initially at 2.5×10^{-3} and then it slowly increases to reach only 5×10^{-3} at the LSO crossing. These (rather small) differences are due to the limited PN knowledge (5PN) at which the residual multipolar amplitudes $\rho_{\ell m}$ are implemented in the radiation reaction. When considering $\nu = 10^{-4}$, still starting at $r_0 = 7$, the picture remains practically unchanged (solid line in the figure), although the difference is slightly larger at the LSO crossing and during the plunge. The cases of $\nu = 10^{-5}$ and $\nu = 10^{-6}$ (that start respectively at $r_0 = 6.3$ and $r_0 = 6.1$) are practically superposed and one sees again a slight increase of the difference around the LSO. This agreement is a strong indication that the analytically resummed radiation-reaction force is suitable to drive the dynamics of a (circularized) EMRI, notably with $\nu = 10^{-6}$, an interesting source for LISA[7]. In the future, it should be explored how this agreement improves when the 14PN-accurate corrections to the $\rho_{\ell m}$ from [103] are included in the flux.

---

[6] Note that the other two apparent vertical lines are actually the junk radiation corresponding to the beginning of the $\nu = 10^{-5}$ and $\nu = 10^{-6}$ simulations.

[7] A similar conclusion was also reached in Refs. [41, 42], that actually pointed out that one should properly calibrate the $\mathcal{F}_\varphi$ function to have an accurate representation of the EMRI dynamics. Note however that here, contrarily to Refs. [41, 42], we include in the discussion also the late inspiral and plunge regime.

As a last remark, Fig. 14 also highlights that the differences between the various curves become smaller and smaller when $\nu \to 0$. In particular, the curves for mass ratios $\nu = 10^{-4,-5,-6}$ are almost superposed, which points out that radiation reaction has little effect during the plunge phase for these binaries. This fact suggests that, when $\nu \lesssim 10^{-4}$, the motion is "quasi-geodesic" around and below LSO crossing [10], i.e., it is a good approximation to the geodesic plunge from the LSO [17, 23, 119].

D. Gravitational recoil

We update the calculation of the $(\nu \to 0)$ recoil velocity performed in Paper I (see also Ref. [9]) using the new data extracted at $\mathscr{I}^+$ and considering more mass ratios. The linear momentum flux emitted in GWs is computed via Eq. (B4) (with $\ell_{\max} = 7$) and is integrated in time to obtain the accumulated complex recoil velocity as

$$v \equiv v_x + \mathrm{i}v_y = v_0 - \frac{1}{M} \int_{t_0}^{t} \left(\mathcal{F}_x^{\mathbf{P}} + \mathrm{i}\mathcal{F}_y^{\mathbf{P}} \right) dt. \qquad (36)$$

Here, t_0 is the initial time of the simulation and v_0 is the initial velocity that the system has acquired from $t = -\infty$ to $t = t_0$. We give a good approximation to v_0 as in Sec. IV of Paper I (and of Ref. [120]), i.e., by determining the center of the hodograph (see Fig. 5 of Paper I) of the complex recoil velocity during part of the inspiral.

Table I lists both the (modulus of) the maximum and the final kick velocity for the five mass ratios considered, together with the total number of orbits, N^{orbits}, and the number of orbits used to determine v_0, N_0^{orbits}. The uncertainty in the numbers is on the last digit (of order $\times 10^{-5}$) and is estimated from the variation of $|v^{\mathrm{end}}|$ and $|v^{\mathrm{max}}|$ when N_0^{orbits} is modified[8]. Note that the values are slightly larger than those of Table III of Paper I, which were measured at $r_*^{\mathrm{extr}}/M = 1000$. Because, as observed before, the dynamics is practically independent on ν for $\nu \le 10^{-4}$, i.e. the motion is quasi-geodesic, we can average the results for $\nu = 10^{-4,-5,-6}$ in Table I so to obtain an estimate of the final and maximum recoil in the $\nu = 0$ case, with an uncertainty given by the corresponding standard deviation. This calculation gives $v_{\mathrm{kick}}^{\mathrm{end}}/(c\nu^2) = 0.04474 \pm 0.00007$ and $v_{\mathrm{kick}}^{\mathrm{max}}/(c\nu^2) = 0.05248 \pm 0.00008$.

---

[8] The perturbative treatment is not meant to give an accurate estimate of the final recoil for $\nu = 10^{-2}$, because high-order, ν-dependent corrections in the dynamics (and waveforms) are important in this case. In fact, the NR simulation of Ref. [6] gives $|v^{\mathrm{end}}|/\nu^2 = 0.037 \pm 0.002$, which is 17% smaller than the perturbative estimate. Nonetheless, the result of Ref. [6] is consistent with the fit analysis of Fig. 7 of Paper I.

TABLE I: Computation of the kick velocity. From left to right, the columns report: the mass ratio ν; the initial separation r_0; the total number of orbits, the number of orbits used to determine an approximate value of the correct initial kick velocity v_0 (see Sec. IV of Paper I); the final kick velocity $|v^{\mathrm{end}}|$ and the maximum kick velocity $|v^{\mathrm{max}}|$.

ν	r_0	N^{orbits}	N_0^{orbits}	$|v^{\mathrm{end}}|/(c\nu^2)$	$|v^{\mathrm{max}}|/(c\nu^2)$
10^{-2}	7.0	6	2	0.0435(6)	0.0508(1)
10^{-3}	7.0	40	14	0.0445(6)	0.0522(8)
10^{-4}	7.0	375	123	0.0447(6)	0.0525(3)
10^{-5}	6.3	349	115	0.0446(6)	0.0523(9)
10^{-6}	6.1	396	133	0.0448(0)	0.0525(2)

VII. CONCLUSIONS

In this paper we discussed, for the first time, the hyperboloidal layer method, introduced in Ref. [100], for the computation of the gravitational radiation emitted by large-mass-ratio compact binaries at null infinity. We used a hyperboloidal layer in a perturbative, time-domain method specifically designed for computing EMR (or IMR) waveforms without the adiabatic assumption. The method employs the RWZ formalism for wave generation and an analytic, EOB-resummed, leading order, radiation reaction for the dynamics of the particle [10, 18, 23, 39, 101]. Higher ν-dependent conservative and nonconservative corrections to the relative dynamics, as present in the complete EOB formalism, are neglected by construction. Merged with the hyperboloidal method, the method efficiently provides accurate waveforms at null infinity. These waveforms have already been used to calibrate effective next-to-quasi-circular corrections to the multipolar EOB-waveform (amplitude and phase) in the test-mass limit [22].

In this paper, beside providing an extensive discussion of the hyperboloidal technique, we presented results concerning the study of the gravitational radiation from circular stable and unstable orbits, and from the coalescence of circularized black-hole binaries with mass ratios $\nu = 10^{-2,-3,-4,-5,-6}$. We improved quantitatively previous work [9, 10, 18, 23], where waves were extracted at finite radii. The difference of the null infinity waveforms to finite-radius and extrapolated waveforms are quantified in detail. The waveforms produced in this work will be made publicly available so to be used in data-analysis pipelines for LISA-type science or for the Einstein Telescope. Below we discuss our results individually, together with an outlook.

Circular orbits. We computed the gravitational energy flux emitted by a particle in geodesic circular motion. We considered a sample of (strong field) circular orbits and found that the flux agrees with the semi-analytic data of Fujita et al. [113] within at most a 0.8% in each multipole. The total flux, summed up to $\ell_{\max} = 8$, agrees

always within 0.02% for all orbits up to the LSO, $r_0 = 6$. We considered also unstable circular orbits, $3.1 \leq r_0 < 6$, which are useful to test the performance of the waveform resummation procedure below the LSO [39]. The Newton-normalized energy flux computed within our approach (considered "exact" for this comparison) is compared with the homologous, EOB-resummed analytic expression. We found a relative difference always below 5% until $r_0 = 4.2$ with a maximum of 10% at $r_0 = 3.3$. We also computed from the numerical data the "exact" residual waveform amplitudes $\rho_{\ell m}^{\text{Exact}}$ introduced in [39], although we did not provide a thorough comparison with their 5PN-accurate analytic counterparts [101].

High accuracy inspiral waveforms at null infinity. We computed high accuracy waveforms covering the complete transition from a (long, ~ 400 orbits for 3 mass ratios) quasi-circular inspiral to plunge, merger and ringdown phases. The phase and amplitude error bars on the dominant multipoles, as estimated from convergence tests, are $\delta\phi \sim 10^{-6}$ and $\delta A/A \sim 10^{-6}$. The multipolar structure of the gravitational wave is qualitatively the same as reported in Paper I and II.

Self-consistency of the method. The perturbative method proposed here has systematic uncertainties in the assumption made for the radiation reaction. To check the self-consistency of our method we compared the mechanical angular momentum loss and the angular momentum flux computed from the waves. For $\nu \leq 10^{-3}$, the relative disagreement between the two is $\sim 2.5 \times 10^{-3}$ at the beginning of the simulations and reaches only $\sim 5 \times 10^{-3}$ at the LSO crossing, which is then maintained up to orbital frequency $M\Omega \sim 0.085$. This agreement supports the reliability of the analytical resummed radiation reaction model.

Comparison with finite radii extraction. We found significant differences in waveforms at finite-radii and at $\mathscr{I}^+$. For example, the $\ell = m = 2$ multipole extracted at $r_*^{\text{extr}}/M = 250$ differs from the $\mathscr{I}^+$ waveform (on average) by $\Delta\phi_{22} \sim 0.1$ rad and by $\Delta A_{22}/A_{22} \sim 0.2\%$ during the late-inspiral and plunge; the differences reduce to $\Delta\phi_{22} \sim 0.025$ rad and $\Delta A_{22}/A_{22} \sim 0.01\%$ at $r_*^{\text{extr}}/M = 1000$. Such differences, though small, are relevant in the comparison with the EOB-resummed analytic waveform [22].

Extrapolation to infinite extraction radius. We extrapolated the finite-radius waveforms to infinite radius using a simple $1/r$-polynomial expression, Eq. (35), as routinely applied to NR waveforms. Considering the $\ell = m = 2$ waveform, we found that the dephasing between the extrapolated and the $\mathscr{I}^+$ waveforms reaches 10^{-3} rad using a linear polynomial in $1/r$ and extraction radii below $1000M$. In our setup, the dephasing can be made small to the level of our uncertainties, by simply improving the extrapolation procedure: for example, it drops to 10^{-6} using larger radii (up to $4000M$) and higher powers ($K = 5$) in the extrapolation. Note that we work within perturbation theory where a fixed, explicitly spherically symmetric background is given. In

NR, the extrapolation procedure is not as well-defined due to various factors such as the (arbitrary) definition of a retarded time, the negligence of gauge dynamics, the identification of a fiducial background, and the use of coordinate spheres. Consequently, the dephasings can be several orders of magnitude larger for NR waveforms of coalescing black-hole binaries [55, 118]. This observation emphasizes the importance of using unambiguous extraction procedures to compute NR waveforms at $\mathscr{I}^+$, such as the CCE implemented by Ref. [55].

Gravitational recoil. We updated the final recoil computed in Paper I and in Ref. [9]. We computed the maximum and final kick for several mass ratios (see Table (I)) and then extrapolated these values to the $\nu \to 0$ limit. Our final estimates for the maximum and final recoil velocities are $v_{\text{kick}}^{\text{max}}/(c\nu^2) = 0.05248 \pm 0.00008$ and $v_{\text{kick}}^{\text{end}}/(c\nu^2) = 0.04474 \pm 0.00007$. These values can be used together with NR data to provide fitting formulas valid for all values of ν (see Paper I).

Outlook. An important development that is called for the future is the computation of the gravitational radiation emitted in the coalescence of *noncircularized* binary systems. In the IMR regime, these systems might be interesting sources for the Einstein Telescope or for planned space interferometers. Within the EOB approach, there are prescriptions [121, 122] to resum the radiation reaction in the noncircularized case and to account for the radiation-reaction driven evolution of the eccentricity. Such prescriptions (in their $\nu = 0$ limit) can be easily implemented in our framework and we plan to do it in a future study.

It will be interesting to motivate *analytically* the behavior of the residual (numerical) amplitudes $\rho_{\ell m}^{\text{Exact}}$ along the sequence of unstable circular orbits. To do so, it will be necessary to compare our results with the 14PN-accurate analytical expressions recently obtained by Fujita [103]. The assessment of the accuracy of the analytical $\rho_{\ell m}$'s for unstable orbits might then be useful to study the dynamical modification to geodesic zoom-whirl orbits due to the action of (EOB-resummed) radiation reaction.

Such studies would also benefit from technical improvements of the finite-difference, time-domain RWZ infrastructure. Possible improvements for the future are the implementation of horizon-penetrating coordinates to increase efficiency and remove reflections from the inner boundary, a better implementation of the initial data that satisfies the linearized Einstein constraint equations, and the use of higher order finite-difference methods to reduce numerical truncation error. One can also extend our numerical framework to spinning black holes by solving, instead of the RWZ equation, the Teukolsky equation for computing the gravitational waves emitted by a small black hole inspiraling into a rotating black hole.

The waveforms produced in this work can be used as a benchmark for the consistency of NR results in the large mass ratio limit [6, 7].

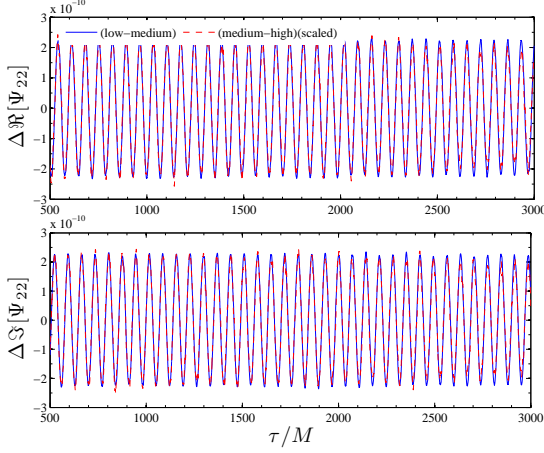Finally, we hope that this work will motivate future

FIG. 15: Convergence of real (top) and imaginary (bottom) part of the $\ell = m = 2$ waveform generated by a particle on a circular orbit at $r_0 = 7.9456$. The plots show the differences between low and medium resolution data and the difference between medium and high resolution data scaled for 4th order convergence.

efforts towards a full understanding of the hyperboloidal initial value problem in nonlinear general relativity, with particular attention to its application in numerical relativity.

Acknowledgments

Appendix A: Convergence tests and errorbars

In this Appendix we present the convergence tests and an estimate of the errors on our data to validate our numerical approach. We observe the expected 4th order convergence, but also a progressive degradation of the quality of data relative to sub-dominant multipoles with $\ell > 6$ and decreasing index $m \ll \ell$. In the following we consider the domain $[\rho_{\min}, S]_{R_*} = [-50, 70]_{50}$ discretized with $N = \{3001, 6001, 12001\}$ points, that correspond to low, medium and high resolution. All data discussed in the bulk of the paper were obtained using the high resolu-

TABLE II: Gravitational energy and angular momentum fluxes at $\mathscr{I}^+$ for a particle on a circular orbit of radius $r_0 = 7.9456$. Compare with Refs. [106, 114].

ℓ	m	$\dot{E}/\nu^2$	$\dot{J}/\nu^2$
2	1	8.1632×10^{-7}	1.8283×10^{-5}
2	2	1.7065×10^{-4}	3.8220×10^{-3}
3	1	2.1740×10^{-9}	4.8691×10^{-8}
3	2	2.5203×10^{-7}	5.6448×10^{-6}
3	3	2.5481×10^{-5}	5.7070×10^{-4}
4	1	8.4001×10^{-13}	1.8814×10^{-11}
4	2	2.5112×10^{-9}	5.6243×10^{-8}
4	3	5.7777×10^{-8}	1.2940×10^{-6}
4	4	4.7289×10^{-6}	1.0591×10^{-4}
5	1	1.2612×10^{-15}	2.8248×10^{-14}
5	2	2.7925×10^{-12}	6.2543×10^{-11}
5	3	1.0948×10^{-9}	2.4520×10^{-8}
5	4	1.2334×10^{-8}	2.7625×10^{-7}
5	5	9.4660×10^{-7}	2.1201×10^{-5}
6	1	2.9141×10^{-19}	6.4421×10^{-18}
6	2	1.3368×10^{-14}	2.9940×10^{-13}
6	3	1.9677×10^{-12}	4.4070×10^{-11}
6	4	3.5023×10^{-10}	7.8442×10^{-9}
6	5	2.5728×10^{-9}	5.7623×10^{-8}
6	6	1.9621×10^{-7}	4.3944×10^{-6}
7	1	$\ldots$	$\ldots$
7	2	9.2734×10^{-18}	2.0765×10^{-16}
7	3	1.7446×10^{-14}	3.9073×10^{-13}
7	4	8.2034×10^{-13}	1.8373×10^{-11}
7	5	9.7500×10^{-11}	2.1837×10^{-9}
7	6	5.3226×10^{-10}	1.1921×10^{-8}
7	7	4.1412×10^{-8}	9.2750×10^{-7}
8	1	$\ldots$	$\ldots$
8	2	2.8445×10^{-20}	5.7900×10^{-19}
8	3	2.1027×10^{-17}	4.7089×10^{-16}
8	4	1.0914×10^{-14}	2.4445×10^{-13}
8	5	2.6777×10^{-13}	5.9973×10^{-12}
8	6	2.5186×10^{-11}	5.6409×10^{-10}
8	7	1.0979×10^{-10}	2.4590×10^{-9}
8	8	8.8253×10^{-9}	1.9766×10^{-7}

tion. The Courant factor is $\alpha_{\rm cfl} = 0.5$, the Kreiss–Oliger dissipation factor is $\sigma = 0.007$, the mass ratio considered for the tests is $\nu = 10^{-2}$, and the waves are extracted at $\mathscr{I}^+$. In the following plots we use the coordinate time τ on the horizontal axis.

We start by considering the waveforms emitted by a particle in stable circular orbits (no radiation reaction) at $r_0 = 7.9456$. This value of the radius is chosen here because it allows for an immediate comparison with published information [106, 114]. Figure 15 shows the dif-

ferences between low and medium resolution data and the difference between medium and high resolution data scaled for 4th order convergence (scaling factor, $s = 16$) of the real (top panel) and the imaginary (bottom panel) part of the $\ell = m = 2$ waveform. The differences are superposed, thus indicating that the code converges at the correct rate. The plot does not show the initial junk radiation, but only the part of the wave that is used below to calculate the GW energy flux. The behavior remains the same for all the subdominant multipoles. For multipoles $\ell \geq 4$ and $m \to 1$ however the amplitude of the solution becomes smaller and smaller (e.g. $|\Psi_{61}| = A_{61} \simeq 10^{-11}$), until it becomes at the same order as round-off numerical noise, and thus cannot be disentangled from it. In addition, such small-amplitude waves can also be polluted by reflections of the initial junk radiation (that remain always of the same order of magnitude for each multipole) from the internal boundary. In order to obtain cleaner data and to estimate the convergence rate in these cases, we smooth the corresponding waves with a digital polynomial filter. The measurement of the convergence rate, however, becomes progressively more difficult for $\ell \geq 4$ and, even with the smoothing, the $(8,1)$ and $(7,1)$ modes are completely polluted by high-frequency noise. Increasing the artificial dissipation in the code does not improve the results. In the future we shall investigate the possibility of reducing the initial junk radiation by improving the initial data set up. We shall also consider the use of higher-order differential operators.

We recall, however, that the higher ℓ modes are progressively less relevant for the total waveform.

We finally list in Table II the values of the GW energy and angular momentum fluxes emitted at $r_0 = 7.9456$, to be compared with published data [106, 114]. The differences with the spectral data of Fujita et al. [113, 123] are below 0.8 % for each multipoles except for the multipoles $(7,7)$ (2.2 %), $(8,7)$ (2.1 %) and $(8,8)$ (4.8 %). We omit the values for multipoles $(7,1)$ and $(8,1)$ since they are not reliable.

Now we discuss some general features of the multipolar waveforms through transition from quasi-circular inspiral to plunge, merger and ringdown. The particle is initially at $r_0 = 7$. The complete $\ell = m = 2$ waveform, real (solid line) and imaginary part (dashed line) is displayed in the top-right inset of Fig. 16. The main panel highlights the structure of the ringdown for the $\ell = m = 2$ and the $\ell = 6$, $m = 1$ modes. In the bottom-left inset of the figure we show the time-evolution of the radial r_* coordinate of the particle: It is initially at $r_* = 8.8326$ and ends at $r_* = \rho_{\min} = -50$. When the particle gets to $\rho_{\min}$ it is advected out of the grid, so that the RWZ source becomes zero for the rest of evolution [10, 18, 23]. This jump in the source can introduce some artifacts in the ringdown waveform and thus the location of $\rho_{\min}$ should be chosen to minimize these effects. From the left-bottom inset of Fig. 16 one sees that $r_* = -50$ at $t_{\text{exit}} \approx 642$. Since the speed of outgoing characteristics is 1 on the layer by construction (see Eq. (11)), a signal generated at $\rho_{\min} = -50$
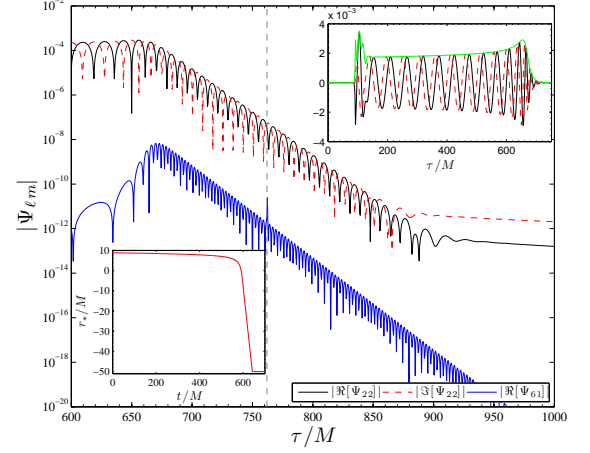

FIG. 16: (Color online) Multipolar waveforms generated by the quasi-circular inspiral, plunge, merger and ringdown of the $\nu = 10^{-2}$ binary initially at separation $r_0 = 7$. Main panel: the ringdown phase for the $\ell = m = 2$ and $\ell = 6$, $m = 1$ modes. Top-right inset: the complete $\ell = m = 2$ waveform. Bottom-left inset: the time-evolution of the r_* coordinates of the point particle. The vertical dashed line on the main panel marks the hyperboloidal time $\tau_{\text{end}} \approx 762$ corresponding to the dynamical time t where the particle reaches the internal boundary of the numerical grid, $\rho_{\min} = -50$.
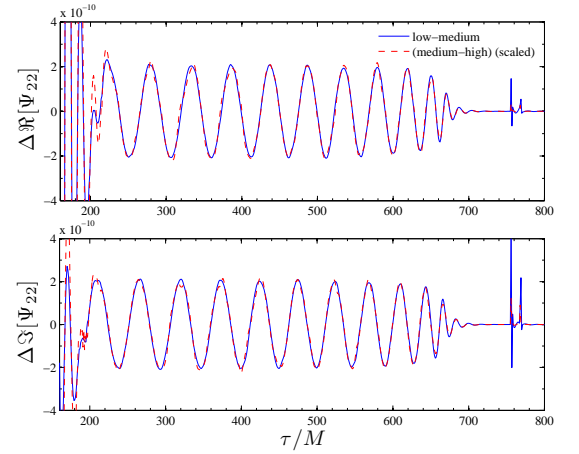

FIG. 17: Same as Fig. 15 but for a particle in a inspiral to plunge orbit.

will take a time $70 - (-50) = 120$ to reach $\mathscr{I}^+$. This means that any signal connected with the particle exiting the domain will show up on the waveform at $\mathscr{I}^+$ at hyperboloidal time $\tau_{\text{exit}} = t_{\text{exit}} + 120 = 762$. This time is marked by the vertical dashed line in Fig. 16. There is no evidence of pathological features in the $\ell = m = 2$ ringdown, but a localized spike is seen in the (much smaller amplitude) $\ell = 6$, $m = 1$ multipole exactly at $\tau = \tau_{\text{exit}}$. By inspecting all multipoles, we found that the effect is always present when the waveform amplitude becomes
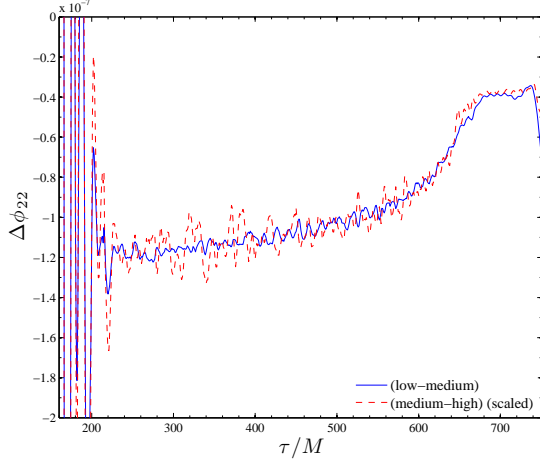
FIG. 18: Convergence of the phase of the $\ell = m = 2$ waveform for inspiral to plunge orbit. The plot shows the differences between low and medium resolution data and the difference between medium and high resolution data scaled for 4th order convergence.

sufficiently small, e.g. for the $m \to 1$ multipoles. Evidently, decreasing $\rho_{\min}$ (e.g., $\rho_{\min} = -200$) would delay the occurrence of this spike, but not remove it, because it is connected to our treatment of the particle and the coordinates that we use (this problem should be solved in horizon-penetrating coordinates). The choice of $\rho_{\min} = -50$ is a reasonable compromise between efficiency and accuracy.

We computed the decay rate of the tail of the $\ell = m = 2$ waveform. A linear fit to the initial part of the tail visible in Fig. 16 gave around -4.5. This finding is in agreement with Fig. 6 of [86], which solved the homogeneous RWZ in quadruple precision and 8th order finite differencing. The tail decay rate is expected to approach the theoretical value $-(\ell + 2) = -4$ asymptotically in time.

The convergence of the $\ell = m = 2$ waveform is demonstrated in Fig. 17, that is the analogue of Fig. 15. As expected, 4th order convergence is observed through inspiral, plunge, and merger phases, as well as during a considerable part of the ringdown. After time $\tau \approx 760$, one can notice the boundary effect mentioned above.

For the discussion in Sec. VI B 1 it is important to establish an error estimate for the gravitational wave phase. Figure 18 shows the convergence test on this quantity. The difference between the low and medium resolution is around $\Delta\phi_{22} \lesssim 10^{-7}$. Using Richardson extrapolation in resolution we estimate the error bars as $\delta\phi_{22} \sim 10^{-6}$ and

$\delta A_{22}/A_{22} \sim 10^{-6}$. We found similar results also for the other multipoles, when possible, to establish the convergence rate. As in the case of circular orbits, results are subjected to a progressive degradation for sub-dominant modes $\ell \geq 6$.

Appendix B: Asymptotic formulas

In this appendix we summarize the relations between the RWZ master functions and the asymptotic observable quantities. From $\Psi_{\ell m}^{(e/o)}$, the h_+ and $h_\times$ GW polarizations are obtained as

$$\mathcal{R}\left(h_+ - ih_\times\right) = \sum_{\ell \geq 2, m}^{\ell_{\max}} \sqrt{\frac{(\ell+2)!}{(\ell-2)!}} \left(\Psi_{\ell m}^{(e)} + i\Psi_{\ell m}^{(o)}\right) {}_{-2}Y^{\ell m},$$
(B1)

where $\mathcal{R}$ is the distance from the source, $\ell_{\max}$ is the maximum number of multipoles one sums over (omitted for brevity in the following sums) , and ${}_{-2}Y^{\ell m} \equiv {}_{-2}Y^{\ell m}(\theta, \varphi)$ are the $s = -2$ spin-weighted spherical harmonics. All second-order quantities follow. The emitted power,

$$\dot{E} = \frac{1}{16\pi} \sum_{\ell \geq 2, m} \frac{(\ell+2)!}{(\ell-2)!} \left(\left|\dot{\Psi}_{\ell m}^{(o)}\right|^2 + \left|\dot{\Psi}_{\ell m}^{(e)}\right|^2\right),$$
(B2)

the angular momentum flux

$$\dot{J} = -\frac{1}{8\pi} \sum_{\ell \geq 2, m > 0} m\frac{(\ell+2)!}{(\ell-2)!}\Im\left[\dot{\Psi}_{\ell m}^{(e)}\Psi_{\ell m}^{(e)*} + \dot{\Psi}_{\ell m}^{(o)}\Psi_{\ell m}^{(o)*}\right],$$
(B3)

that is obtained from the corresponding relation of Paper I using $\Psi_{\ell m}^* = (-1)^m\Psi_{\ell,-m}$, so that the sum is performed only over $0 < m \leq \ell$ multipoles, and the linear momentum flux [120, 124, 125],

$$\mathcal{F}_x^{\mathbf{P}} + i\mathcal{F}_y^{\mathbf{P}} = \frac{1}{8\pi} \sum_{\ell \geq 2, m} \left[ia_{\ell m}\dot{\Psi}_{\ell m}^{(e)}\dot{\Psi}_{\ell,m+1}^{(o)*}\right.$$
$$\left. + b_{\ell m}\left(\dot{\Psi}_{\ell m}^{(e)}\dot{\Psi}_{\ell+1,m+1}^{(e)*} + \dot{\Psi}_{\ell m}^{(o)}\dot{\Psi}_{\ell+1,m+1}^{(o)*}\right)\right],$$
(B4)

where

$$a_{\ell m} = 2(\ell-1)(\ell+2)\sqrt{(\ell-m)(\ell+m+1)},$$
(B5)

$$b_{\ell m} = \frac{(\ell+3)!}{(\ell+1)(\ell-2)!}\sqrt{\frac{(\ell+m+1)(\ell+m+2)}{(2\ell+1)(2\ell+3)}}.$$
(B6)

[1] http://lisa.nasa.gov.
[2] http://www.esa.int/science/lisa.
[3] M. Punturo, M. Abernathy, F. Acernese, B. Allen, N. Andersson, et al., Class.Quant.Grav. **27**, 194002

(2010).
[4] B. Sathyaprakash and B. Schutz, Living Rev.Rel. **12**, 2 (2009), 0903.3338.
[5] E. Huerta and J. R. Gair, Phys.Rev. **D83**, 044020

(2011), 1009.1985.

[6] C. O. Lousto and Y. Zlochower (2010), 1009.0292.

[7] U. Sperhake, V. Cardoso, C. D. Ott, E. Schnetter, and H. Witek (2011), 1105.5391.

[8] L. Blanchet, Living Rev.Rel. **9**, 4 (2006).

[9] P. A. Sundararajan, G. Khanna, and S. A. Hughes, Phys.Rev. **D81**, 104009 (2010), 1003.0485.

[10] S. Bernuzzi and A. Nagar, Phys. Rev. **D81**, 084056 (2010), 1003.0597.

[11] M. Davis, R. Ruffini, and J. Tiomno, Phys.Rev. **D5**, 2932 (1972).

[12] C. O. Lousto and R. H. Price, Phys.Rev. **D55**, 2124 (1997), gr-qc/9609012.

[13] M. Davis, R. Ruffini, W. Press, and R. Price, Phys.Rev.Lett. **27**, 1466 (1971).

[14] K. Martel and E. Poisson, Phys.Rev. **D66**, 084001 (2002), gr-qc/0107104.

[15] E. Berti, V. Cardoso, T. Hinderer, M. Lemos, F. Pretorius, et al., Phys.Rev. **D81**, 104048 (2010), 1003.0812.

[16] E. Mitsou, Phys.Rev. **D83**, 044039 (2011), 1012.2028.

[17] S. Hadar, B. Kol, E. Berti, and V. Cardoso (2011), 1105.3861.

[18] A. Nagar, T. Damour, and A. Tartaglia, Class. Quant. Grav. **24**, S109 (2007), gr-qc/0612096.

[19] Y. Mino and J. Brink, Phys.Rev. **D78**, 124015 (2008), 0809.2814.

[20] P. A. Sundararajan, G. Khanna, S. A. Hughes, and S. Drasco, Phys.Rev. **D78**, 024022 (2008), 0803.0317.

[21] P. A. Sundararajan, G. Khanna, and S. A. Hughes, Phys.Rev. **D76**, 104005 (2007), gr-qc/0703028.

[22] S. Bernuzzi, A. Nagar, and A. Zenginoglu, Phys.Rev. **D83**, 064010 (2011), 1012.2456.

[23] T. Damour and A. Nagar, Phys. Rev. **D76**, 064028 (2007), 0705.2519.

[24] L. Barack and N. Sago, Phys. Rev. **D81**, 084021 (2010), 1002.2386.

[25] L. Barack and N. Sago, Phys.Rev.Lett. **102**, 191101 (2009), 0902.0573.

[26] L. Barack, Class.Quant.Grav. **26**, 213001 (2009), 0908.1664.

[27] L. Barack and N. Sago, Phys.Rev. **D83**, 084023 (2011), 1101.3331.

[28] L. Blanchet, S. L. Detweiler, A. Le Tiec, and B. F. Whiting, Phys.Rev. **D81**, 084033 (2010), 1002.0726.

[29] E. Poisson, A. Pound, and I. Vega (2011), 1102.0529.

[30] A. Buonanno and T. Damour, Phys. Rev. **D62**, 064015 (2000), gr-qc/0001013.

[31] A. Buonanno and T. Damour, Phys. Rev. **D59**, 084006 (1999), gr-qc/9811091.

[32] A. Buonanno, Y. Chen, and T. Damour, Phys. Rev. **D74**, 104005 (2006), gr-qc/0508067.

[33] T. Damour, P. Jaranowski, and G. Schaefer, Phys.Rev. **D78**, 024009 (2008), 0803.0915.

[34] E. Barausse and A. Buonanno, Phys.Rev. **D81**, 084024 (2010), 0912.3517.

[35] A. Nagar (2011), * Temporary entry *, 1106.4349.

[36] E. Barausse and A. Buonanno (2011), * Temporary entry *, 1107.2904.

[37] T. Damour and A. Nagar, Phys.Rev. **D81**, 084016 (2010), 0911.5041.

[38] T. Damour, Phys. Rev. **D64**, 124013 (2001), gr-qc/0103018.

[39] T. Damour, B. R. Iyer, and A. Nagar, Phys. Rev. **D79**, 064004 (2009), 0811.2069.

[40] Y. Pan, A. Buonanno, M. Boyle, L. T. Buchman, L. E. Kidder, et al. (2011), 1106.1021.

[41] N. Yunes, A. Buonanno, S. A. Hughes, M. Coleman Miller, and Y. Pan, Phys. Rev. Lett. **104**, 091102 (2010), 0909.4263.

[42] N. Yunes, A. Buonanno, S. A. Hughes, Y. Pan, E. Barausse, et al., Phys.Rev. **D83**, 044044 (2011), 1009.6013.

[43] T. Damour and A. Nagar, Phys. Rev. **D79**, 081503 (2009), 0902.0136.

[44] L. Baiotti, T. Damour, B. Giacomazzo, A. Nagar, and L. Rezzolla (2011), * Temporary entry *, 1103.3874.

[45] A. L. Tiec, A. H. Mroue, L. Barack, A. Buonanno, H. P. Pfeiffer, et al. (2011), * Temporary entry *, 1106.3278.

[46] Y. Pan, A. Buonanno, R. Fujita, E. Racine, and H. Tagoshi, Phys.Rev. **D83**, 064003 (2011), 1006.0431.

[47] M. Boyle et al., Phys. Rev. **D76**, 124038 (2007), 0710.0158.

[48] M. Boyle and A. H. Mroue, Phys. Rev. **D80**, 124045 (2009), 0905.3177.

[49] M. Boyle, A. Buonanno, L. E. Kidder, A. H. Mroue, Y. Pan, et al., Phys.Rev. **D78**, 104020 (2008), 0804.4184.

[50] D. Pollney, C. Reisswig, N. Dorband, E. Schnetter, and P. Diener, Phys. Rev. **D80**, 121502 (2009), 0910.3656.

[51] D. Pollney, C. Reisswig, E. Schnetter, N. Dorband, and P. Diener, Phys.Rev. **D83**, 044045 (2011), 0910.3803.

[52] N. T. Bishop, R. Gomez, L. Lehner, and J. Winicour, Phys.Rev. **D54**, 6153 (1996).

[53] M. Babiuc, B. Szilagyi, I. Hawke, and Y. Zlochower, Class.Quant.Grav. **22**, 5089 (2005), gr-qc/0501008.

[54] M. Babiuc, N. Bishop, B. Szilagyi, and J. Winicour, Phys.Rev. **D79**, 084011 (2009), 0808.0861.

[55] C. Reisswig, N. Bishop, D. Pollney, and B. Szilagyi, Phys.Rev.Lett. **103**, 221101 (2009), 0907.2637.

[56] C. Reisswig, N. T. Bishop, D. Pollney, and B. Szilagyi, Class. Quant. Grav. **27**, 075014 (2010), 0912.1285.

[57] M. Babiuc, J. Winicour, and Y. Zlochower, Class.Quant.Grav. **28**, 134006 (2011), 1106.4841.

[58] N. Bishop, D. Pollney, and C. Reisswig (2011), 1101.5492.

[59] H. Friedrich, Comm. Math. Phys. **91**, 445 (1983).

[60] D. M. Eardley and L. Smarr, Phys.Rev. **D19**, 2239 (1979).

[61] D. R. Brill, J. M. Cavallo, and J. A. Isenberg, Journal of Mathematical Physics **21**, 2789 (1980).

[62] L. Smarr and J. York, James W., Phys.Rev. **D17**, 2529 (1978).

[63] R. H. Gowdy, J. Math. Phys. **22**, 675 (1981).

[64] H. Friedrich, Comm. Math. Phys. **107**, 587 (1986).

[65] J. Frauendiener, Living Rev.Rel. **3**, 4 (2000).

[66] S. Husa, Lect.Notes Phys. **617**, 159 (2003), gr-qc/0204057.

[67] A. Zenginoglu, Class. Quant. Grav. **25**, 195025 (2008), 0808.0810.

[68] V. Moncrief and O. Rinne, Class. Quant. Grav. **26**, 125010 (2009), 0811.4109.

[69] J. M. Bardeen, O. Sarbach, and L. T. Buchman, Phys.Rev.D (2011), 1101.5479.

[70] O. Rinne, Class. Quant. Grav. **27**, 035014 (2010), 0910.0139.

[71] J. Frauendiener, Phys. Rev. D **58**, 064003 (1998), gr-qc/9712052.

[72] V. Moncrief, *Conformally regular ADM evolution equations* (2000), talk at Santa Barbara,

http://online.itp.ucsb.edu/online/numrel00/moncrief.

[73] G. Fodor and I. Racz, Phys. Rev. Lett. **92**, 151801 (2004), hep-th/0311061.

[74] P. Bizon and A. Zenginoglu, Nonlinearity **22**, 2473 (2009), 0811.3966.

[75] G. Fodor and I. Racz, Phys.Rev. **D77**, 025019 (2008), hep-th/0609110.

[76] J. R. van Meter, D. R. Fiske, and C. W. Misner, Phys. Rev. **D74**, 064003 (2006), gr-qc/0603034.

[77] A. P. Gentle, D. E. Holz, A. Kheyfets, P. Laguna, W. A. Miller, et al., Phys.Rev. **D63**, 064024 (2001), gr-qc/0005113.

[78] R. H. Gowdy (2001), gr-qc/0107016.

[79] B. G. Schmidt, in *The Conformal Structure of Space-times: Geometry, Analysis, Numerics*, edited by J. Frauendiener and H. Friedrich (Springer, 2002), vol. 604 of *Lecture Notes in Physics*, pp. 283–295.

[80] G. Calabrese, C. Gundlach, and D. Hilditch, Class.Quant.Grav. **23**, 4829 (2006), gr-qc/0512149.

[81] A. Zenginoglu, Class. Quant. Grav. **25**, 145002 (2008), 0712.4333.

[82] A. Zenginoglu and M. Tiglio, Phys. Rev. **D80**, 024044 (2009), 0906.3342.

[83] A. Zenginoglu, Class. Quant. Grav. **25**, 175013 (2008), 0803.2018.

[84] P. Bizon, A. Rostworowski, and A. Zenginoglu, Class. Quant. Grav. **27**, 175003 (2010), 1005.1708.

[85] A. Zenginoglu and L. E. Kidder, Phys. Rev. **D81**, 124010 (2010), 1004.0760.

[86] A. Zenginoglu, Class. Quant. Grav. **27**, 045015 (2010), 0911.2450.

[87] A. Zenginoglu, D. Nunez, and S. Husa, Class. Quant. Grav. **26**, 035009 (2009), 0810.1929.

[88] J. A. Gonzalez, F. S. Guzman, and O. Sarbach, Phys. Rev. **D80**, 024023 (2009), 0906.0420.

[89] F. Lora-Clavijo, A. Cruz-Osorio, and F. Guzman, Phys.Rev. **D82**, 023005 (2010), 1007.1162.

[90] I. Vega, B. Wardell, and P. Diener, Class.Quant.Grav. **28**, 134010 (2011), 1101.2925.

[91] I. Racz and G. Z. Toth (2011), 1104.4199.

[92] K. Martel and E. Poisson, Phys. Rev. **D71**, 104003 (2005), gr-qc/0502028.

[93] T. Regge and J. A. Wheeler, Phys.Rev. **108**, 1063 (1957).

[94] F. J. Zerilli, Phys.Rev.Lett. **24**, 737 (1970).

[95] A. Nagar and L. Rezzolla, Class.Quant.Grav. **22**, R167 (2005), gr-qc/0502064.

[96] O. Sarbach and M. Tiglio, Phys. Rev. **D64**, 084016 (2001), gr-qc/0104061.

[97] P. Papadopoulos and J. A. Font, Phys.Rev. **D63**, 044016 (2001), gr-qc/0009024.

[98] A. Nagar, J. A. Font, O. Zanotti, and R. De Pietri, Phys.Rev. **D72**, 024007 (2005), gr-qc/0506070.

[99] A. Nagar, O. Zanotti, J. A. Font, and L. Rezzolla, Phys.Rev. **D75**, 044016 (2007), gr-qc/0610131.

[100] A. Zenginoglu, J.Comput.Phys. **230**, 2286 (2011), 1008.3809.

[101] R. Fujita and B. R. Iyer, Phys. Rev. **D82**, 044051 (2010), 1005.2266.

[102] T. Damour and A. Gopakumar, Phys. Rev. **D73**, 124006 (2006), gr-qc/0602117.

[103] R. Fujita (2011), 1104.5615.

[104] C. E. Grosch and S. A. Orszag, J. Comput. Phys. **25**, 273 (1977).

[105] A. Zenginoglu, Phys. Rev. **D83**, 127502 (2011), 1102.2451.

[106] K. Martel, Phys.Rev. **D69**, 044025 (2004), gr-qc/0311017.

[107] R. Penrose, Phys. Rev. Lett. **10**, 66 (1963).

[108] R. Penrose, Proc. Roy. Soc. Lond. **A284**, 159 (1965).

[109] G. Calabrese and C. Gundlach, Class. Quant. Grav. **23**, S343 (2006), gr-qc/0509119.

[110] S. E. Field, J. S. Hesthaven, and S. R. Lau, Phys. Rev. **D81**, 124030 (2010), 1001.2578.

[111] P. Canizares, C. F. Sopuerta, and J. L. Jaramillo, Phys. Rev. **D82**, 044023 (2010), 1006.3201.

[112] J. L. Jaramillo, C. F. Sopuerta, and P. Canizares, Phys.Rev. **D83**, 061503 (2011), 1101.2324.

[113] R. Fujita and H. Tagoshi, Prog.Theor.Phys. **112**, 415 (2004), gr-qc/0410018.

[114] C. F. Sopuerta and P. Laguna, Phys.Rev. **D73**, 044028 (2006), gr-qc/0512028.

[115] C. Cutler, E. Poisson, G. Sussman, and L. Finn, Phys.Rev. **D47**, 1511 (1993).

[116] J. Pons, E. Berti, L. Gualtieri, G. Miniutti, and V. Ferrari, Phys.Rev. **D65**, 104021 (2002), gr-qc/0111104.

[117] N. Yunes and E. Berti, Phys.Rev. **D77**, 124006 (2008), 0803.1853.

[118] M. A. Scheel et al., Phys. Rev. **D79**, 024003 (2009), 0810.1767.

[119] S. Hadar and B. Kol (2009), 0911.3899.

[120] D. Pollney et al., Phys. Rev. **D76**, 124002 (2007), 0707.2559.

[121] T. Damour, A. Gopakumar, and B. R. Iyer, Phys.Rev. **D70**, 064028 (2004), gr-qc/0404128.

[122] T. Damour, A. Gopakumar, and B. R. Iyer, Class.Quant.Grav. **22**, S381 (2005).

[123] R. Fujita, W. Hikida, and H. Tagoshi, Prog.Theor.Phys. **121**, 843 (2009), 0904.3810.

[124] K. S. Thorne, Rev. Mod. Phys. **52**, 299 (1980).

[125] M. Ruiz, R. Takahashi, M. Alcubierre, and D. Nunez, Gen. Rel. Grav. **40**, 2467 (2008), 0707.4654.